

# A new equation of state applied to planetary impacts

## II. Lunar-forming impact simulations with a primordial magma ocean

Robert Wissing<sup>1,2</sup> and David Hobbs<sup>1</sup>

<sup>1</sup> Lund Observatory, Department of Astronomy and Theoretical Physics, Lund University, Box 43, 22100 Lund, Sweden  
e-mail: david@astro.lu.se

<sup>2</sup> Institute of Theoretical Astrophysics, University of Oslo, Postboks 1029, 0315 Oslo, Norway  
e-mail: robertwi@astro.uio.no

Received 2 July 2019 / Accepted 11 August 2020

### ABSTRACT

Observed FeO/MgO ratios in the Moon and Earth are inconsistent with simulations done with a single homogeneous silicate layer. In this paper we use a newly developed equation of state to perform smoothed particle hydrodynamics simulations on the lunar-forming impact, testing the effect of a primordial magma ocean on Earth. This is investigated using the impact parameters of both the canonical case, in which a Mars-sized impactor hits a non-rotating Earth at an oblate angle, and the fast-rotating case, in which a half-sized Mars impactor hits a fast-spinning Earth head-on. We find that the inclusion of a magma ocean results in a less massive Moon and leads to slightly more mixing. Additionally, we test how an icy Theia would affect the results and find that this reduces the probability of a successful Moon formation. Simulations of the fast-spinning case are found to be unable to form a massive-enough Moon.

**Key words.** equation of state – planets and satellites: formation – planets and satellites: dynamical evolution and stability – planets and satellites: interiors – Moon – Earth

### 1. Introduction

During the late stages of planet formation, it is believed that the inner Solar System was populated by planetary embryos with masses ranging from 0.01 to 0.2 Earth masses (Mars-like; [Ida & Makino 1993](#)). For a planet to grow much larger than this, collisions between planetary embryos are believed to be necessary ([Goldreich et al. 2004](#)). Several of these giant collisions resulted in the Earth, and the last one is believed to have been the lunar-forming impact ([Hartmann & Davis 1975](#); [Cameron & Ward 1976](#)). In addition to fitting neatly into planetary formation models, this scenario also explains many of the observed physical traits of the Earth–Moon system (i.e., correct Moon mass and angular momentum of the current Earth–Moon system, and the small iron core of the Moon; [Canup & Asphaug 2001](#)). There are several variants and models of the giant impact theory, the most famous one being the “canonical” one ([Benz et al. 1989](#); [Canup 2004](#)), in which a planet called Theia hit the Earth at around a 45-degree impact angle resulting in a disc of material that eventually coalesced into the Moon ([Canup & Asphaug 2001](#)). This model correctly captures many of the dynamical aspects of the Earth–Moon system, but fails to reproduce the isotopic similarity of the Earth and Moon found from observations ([Wiechert et al. 2001](#); [Zhang et al. 2012](#)); in the canonical model, most of the mass that created the Moon came from Theia, which would most likely have had a different isotopic ratio, and certain isotope ratios are very sensitive to their initial birth environment in the protoplanetary disk ([Pahlevan & Stevenson 2007](#)). This has led to other variants of the giant-impact theory, the most prominent ones being: the merger theory ([Canup 2012](#)), which predicts that the Moon formed from the debris left by a merger between two half-sized Earths; the fast-spinning theory ([Čuk & Stewart 2012](#)), in which a smaller Theia collides with a fast-spinning proto-Earth that flung material out to create the

Moon; and the hit-and-run model ([Reufer et al. 2012](#)), in which a substantial amount of Theia escapes orbit, leaving a disc that is less enriched with Theia than in the canonical model. The first two variations are referred to as high-angular-momentum theories as the resulting system has an angular momentum that is far above the one we have today. Fast-spinning theory argues that this is due to subsequent momentum loss caused by evection resonance ([Touma & Wisdom 1998](#); [Čuk & Stewart 2012](#)). These two models produce the correct isotopic ratios, but are problematic when it comes to reproducing the chemical differences between Earth and the Moon. In comparison to Earth, the Lunar mantle is depleted in volatile and siderophile elements ([Jones & Palme 2000](#)), which includes a difference in the content of FeO (Earth: 7.67% vs. Moon: 10.6%; [Warren & Dauphas 2014](#)). Because of the highly mixed end-state of the high-angular-momentum models, this FeO difference cannot have originated from the lunar-forming impact itself and requires either a post-impact self-oxidation of the lunar mantle ([Wade & Wood 2005](#)), oxidation by a late veneer, or chemical fractionation in the post-impact disc ([Pahlevan et al. 2011](#)). It is unlikely that self-oxidation of the lunar mantle or oxidation by a late veneer would be more important on the Moon than on the Earth ([Meier et al. 2014](#)). [Pahlevan et al. \(2011\)](#) showed that chemical fractionation can occur in the post-impact disc due to rainout in convective clouds; however, this requires that the turbulent mixing occur faster than the transfer of angular momentum within the disk ([Melosh 2009](#)), and whether or not this happens is still uncertain. Further post-disc simulations are required to gauge the effect of chemical fractionation. In the case of the canonical model, the chemical difference can be more easily explained because the difference produced depends heavily on the composition of Theia. To obtain the correct isotope ratios in this latter case would require that proto-Earth and Theia have almost identical isotope ratios to begin with; this has been argued to

be the case by some authors (Mastrobuono-Battisti et al. 2015; Dauphas 2017), but is considered unlikely by others (Pahlevan & Stevenson 2007; Kaib & Cowan 2015). Another possible solution was presented by Karato (2014), which suggested that the primordial magma ocean on Earth would have been enriched in FeO as melting changes the chemical composition. If large amounts of magma were flung into orbit, this could explain the richness in FeO that we see in the Moon today. All of the simulations mentioned above only used two homogeneous layers (iron core and silicate mantle) to describe the collision, neglecting the modeling of a magma ocean. Asymmetric shock heating would have been important if the Earth had a molten surface while Theia did not. The liquid has a higher Gruneisen parameter and is more easily compressed than its solid counterpart, leading to asymmetric heating at impact and a higher pressure gradient from the molten surface. From planetary studies, a Mars-like planet like Theia would not have had a molten surface (Sasaki & Nakazawa 1986). While the Earth is predicted to have had a molten surface of at least 300 km in depth (Abe 1997). Our numerical simulations test the effect of a proto-Earth with a molten surface compared to that of a solid surface. The simulations also test a wide array of different impact conditions. This includes simulations done in accordance with the setup of both the canonical case (Canup 2004) and from the fast-spinning case (Čuk & Stewart 2012). In addition, we look at the difference between two models of Theia, a rocky and an icy one. An icy Theia would have had to migrate inward from the outer Solar System, just like Ceres is believed to have done (McKinnon 2008; Walsh et al. 2011). Concurrent to the development of the work presented in this paper, Hosono et al. (2019) presented results from numerical simulations of lunar-forming impacts with a terrestrial magma ocean. We discuss the results of the two models and differences between them in Sect. 5.

In Sect. 2 we explain the setup of the simulations. In Sect. 3 we discuss the post-analysis of the simulations and perform a compositional analysis of the lunar-forming impact. In Sect. 4 the results of our simulations are presented and in Sect. 5 we discuss the different results. We finally end with some conclusions.

## 2. Simulation setup

Simulations of the lunar-forming impact were done using smoothed particle hydrodynamics (SPH; Lucy 1977; Gingold & Monaghan 1977), with the astrophysical code VINE (Wetzstein et al. 2009). The equation of state (EOS) was implemented within VINE and the default internal energy evolution was replaced with a temperature evolution. Material strength can be ignored, as the kinetic energy of the lunar-forming impact exceeds the yield strength of the materials (Asphaug et al. 2015). We use a C4 Wendland kernel that has been shown to be resistant against the pairing instability (Dehnen & Aly 2012). This allows for a higher neighbor count (around 200), which improves the convergence of SPH. To model shock dissipation in SPH the artificial viscosity (AV) switch prescription of Morris & Monaghan (1997) is used.

### 2.1. Planetary models

The density profiles of the different models of proto-Earth and Theia were attained from the same method presented in paper 1. We used eight proto-Earth models in our simulations. This includes either a multi-layered (4 main layers) or a

simple-layered (2 main layers) proto-Earth with either a molten (PEM) or solid (PES) surface with a mass of either  $M_P = 0.95M_E$  or  $M_P = 1.05M_E$ .

The multi-layered PES model consists of four layers, inner core (IC), outer core (OC), lower mantle (LM), and upper mantle (UM). The IC, OC, and LM are taken to be the same as the fitted values from the preliminary reference Earth model (PREM; see paper 1). The UM is taken to be made of olivine, which is the most abundant mineral in Earth’s upper mantle. The central pressure and temperature are taken to be the same as in the PREM model (see paper 1) in order to keep the conditions of the inner regions of the planet roughly the same for all the models. The simple-layered PES model is constructed with only the IC material and the UM material (olivine). To achieve a surface temperature of around 1000 K in both PES models, we add a small temperature discontinuity at the core–mantle boundary.

The multi-layered PEM model consists of exactly the same material layers with the addition of a surface magma layer that has a depth of around 300–500 km (Abe 1997). The magma layer is modeled after the olivine melt. We get the olivine material and melt data from several sources (Stixrude & Lithgow-Bertelloni 2005; Jing & Karato 2011; Thomas et al. 2012; Costa et al. 2017). We use the same central pressure and temperature as the PES model, however we do not include any temperature discontinuity at the core–mantle boundary. The simple-layered PEM model is constructed with only the IC material, the UM material (olivine), and the magma layer. In both models, the surface temperature ends up being around 2000 K.

We also have a test model which is the same as the two-layered model, except with its material vaporization energy set to triple the original value. This is done to gauge the effect of the expanded state model in the EOS.

In the case of Theia, we have three models. Two of these are different in that they have different sizes and mass ( $M = 0.142M_E$ ,  $M = 0.05M_E$ ), which are the same masses as the ones used by Canup (2004) and Čuk & Stewart (2012). These two models consider only two layers, an iron core (modeled as the inner core PREM model) representing a third of the planet’s mass, and an olivine mantle representing the rest. The core pressure and temperature are adjusted to give the desired mass and surface temperature ( $T \approx 1000$  K) of the planet. We call these the rocky Theia models. The theother Theia model represents an “icy” Theia with density and properties modeled based on CI-chondrite meteorites and planetary data from Ceres (Thomas et al. 2005; Park et al. 2016). We make a rather simple model of the “icy” material. CI-chondrites are made out of several different silicates and water-bearing phyllosilicates, with the most abundant silicate being olivine. We decided to determine the material properties of our icy material from a weighted average between olivine and ice from material parameters taken from Stixrude & Lithgow-Bertelloni (2005) and Weppner et al. (2015). We fit the values to a core that has around  $\rho = 2600 \leftrightarrow 2300$  kg m<sup>-3</sup> and a mantle that has around  $\rho = 1600 \leftrightarrow 2000$  kg m<sup>-3</sup>, leaving us with a total bulk density of  $\rho = 2200$  kg m<sup>-3</sup>, just as was measured for Ceres. All the planets and their material layers together with respective ambient pressure values are given in Appendix A.

### 2.2. Distribution of particles

Shells are distributed radially outward by the method described in Appendix B. Given the density profile and a chosen number of particles N, we can determine the number of shells and the number of particles per shell. All our particles have the same mass, as

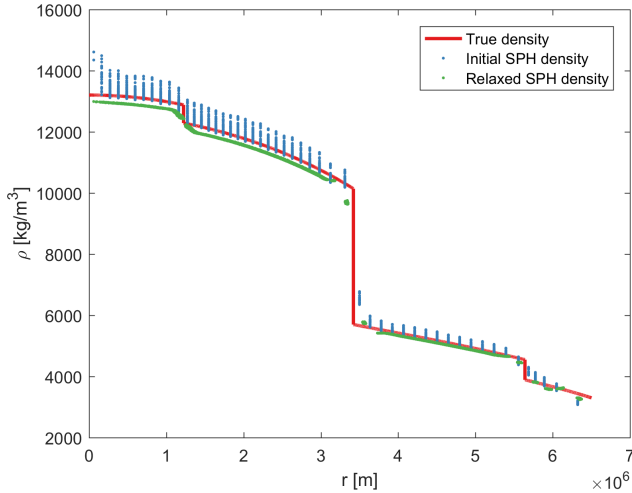


**Fig. 1.** Depiction of the initial condition of the  $M = 1.05M_E$  multi-layered PES model. Here, we show how the true density compares with the approximated density from the SPH summation formula. The initial SPH density is given from the initial distribution of particles using the method described in Appendix B. The density after relaxation is given by the green curve. We can see that in general we get a very good fit; however, we do get a slight gap between the density discontinuities, which is characteristic of the artificial surface tension effect (Agertz et al. 2007).

unequal masses produce numerical artifacts in very mixed cases (Rasio & Lombardi 1999). The particles are distributed in a spiral pattern on the shells following the prescribed method of Saff & Kuijlaars (1997).

Ideally one would like an initial distribution that is isotropic and that follows the true density profile. From Fig. 1 we can see that the distribution follows the density profile quite well. However, the distribution is not completely isotropic: there is a bias near the discontinuities. On the high-density side, the distance to the closest neighbors on the shell is smaller than the distance to the closest neighbors between shells. The opposite is true on the low-density side. However, without changing the particle masses or implementing first-order corrections to the kernel (Reinhardt & Stadel 2017) this small bias in the initial distribution is more desirable than a poor density fit. Letting the distribution relax and equilibrate will minimize the bias. The distribution is relaxed until the mean speed of the particles is below a fraction of the impact speed ( $\langle v_P \rangle < 0.01|v_{\text{imp}}|$ ). From Fig. 1 we can see that doing the relaxation of our planet gives a good fit to the planet’s true density profile despite having several density discontinuities to deal with.

To investigate the effect of rotation in impacts, we also add spin to our proto-Earth models. For the sake of comparison, we choose the rotations based on the ones used by Čuk & Stewart (2012). We spin up the planets by incrementally adding angular momentum to the planet and letting it relax. This is done to reduce any unwanted particle disorder and to reduce the error in the total energy. We begin by spinning it up to a period of 6h, then further to 3, 2.5, and finally to 2.3 h<sup>1</sup>. When relaxing the rotating planet we instead stop the relaxation when the z-component of the velocity goes to a fraction of the impact speed. The flattening and equatorial radius of the spun up proto-Earth are  $f = \frac{R_{\text{eq}} - R_{\text{pole}}}{R_{\text{eq}}} \approx 0.5$  and  $R_{\text{eq}} = 8500$  km respectively,

<sup>1</sup> The spin period is approximate, specifically the spin of the planet is fitted to the angular momentum given in Čuk & Stewart (2012).

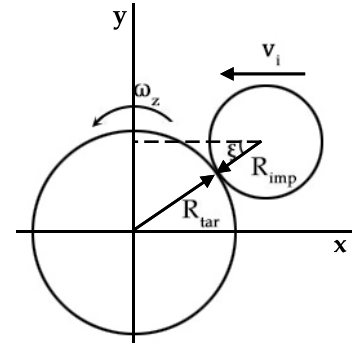


**Fig. 2.** Top-down view of an impact, highlighting the important parameters involved in the collision.

which is in line with the initial conditions from Čuk & Stewart (2012).

### 2.3. Impact parameters

The collision is set up as seen in Fig. 2. The target planet is denoted with subscript “tar” and the impactor is denoted with subscript “imp”. Other than the mass ( $M_{\text{tar}}, M_{\text{imp}}$ ), radius ( $R_{\text{tar}}, R_{\text{imp}}$ ), and material properties of the two bodies (Appendix A), there are three important parameters to consider. The first is the velocity at impact  $v_{\text{imp}}$ :

$$v_{\text{imp}}^2 = v_{\text{esc}}^2 + v_{\text{inf}}^2, \quad (1)$$

where  $v_{\text{esc}}$  is the escape velocity, which is the velocity that a body would attain from just the gravitational attraction of the other, if they started out at rest and infinitely far apart from each other, and  $v_{\text{inf}}$  is the velocity at infinity which is any excess velocity that the body might have gained apart from the escape velocity. The second important parameter is the angle between the two planetary surfaces at the point of impact  $\xi$ , which is often written as an impact parameter  $b$ :

$$b = \sin(\xi). \quad (2)$$

The third involves the spin of the target planet  $\omega_z$  (or impactor) around the equatorial plane  $z$ . The spin can either be prograde or retrograde. We set up our spin on the planets such that  $b > 0$  represents prograde impacts and  $b < 0$  represents retrograde impacts. All of our impacts are aligned to the equatorial plane of the target planet  $z = 0$ .

We either choose  $v_{\text{imp}}$  and  $b$  directly, or we infer  $v_{\text{imp}}$  by choosing  $b$  and a desired angular momentum for the impact:

$$L_{\text{imp}} = L_{\text{col}} + L_{\omega}, \quad (3)$$

where  $L_{\text{imp}}$  is the total angular momentum involved in the impact,  $L_{\text{col}}$  represents the initial orbital angular momentum, and  $L_{\omega}$  represent the spin angular momentum of the planets. By setting a desired  $L_{\text{imp}}$  we can then get  $v_{\text{imp}}$  from  $L_{\text{col}}$  (Canup 2008a).

## 3. Impact analysis

The success of an impact is evaluated based on constraints given by the current Earth–Moon system.

1. The resulting planet ( $M_P$ ) and satellite ( $M_m$ ) must have a mass similar to that of Earth ( $M_E = 5.98 \times 10^{24}$  kg) and the Moon ( $M_M = 7.35 \times 10^{22}$  kg).

2. The final angular momentum must be greater than or equal to the current Earth–Moon system ( $L_{EM} = 3.5 \times 10^{34} \text{ kg m}^2 \text{ s}^{-1}$ )<sup>2</sup>.
  3. The resulting satellite must replicate the iron deficiency of the Moon ( $\delta_{FE} < 10\%$ ).
  4. Given the isotopic composition of Theia, the impact must reproduce the similarity in isotopic ratios of the Earth and the Moon ( $\delta f_T$ ).
  5. The resulting planet and satellite must have plausible relative FeO/MgO ratios for proto-Earth ( $Q_{tar,solid}$ ) and Theia ( $Q_{imp}$ ).
- After the impact, a disk of material will form around the Earth. A fraction of the material in the disk will eventually coalesce and form the Moon. The subsequent viscous evolution of the disk is not simulated; instead we use the empirical results of [Ida et al. \(1997\)](#); [Kokubo et al. \(2000\)](#) to determine the mass of the Moon.

$$M_m = \frac{1.9L_D}{\sqrt{2.9GM_E R_E}} - 1.1M_D - 1.9M_{D,esc}, \quad (4)$$

where  $M_D$  and  $L_D$  are the mass and angular momentum of the disk, respectively, and  $M_{D,esc}$  is the estimated mass that is lost during its evolution. This latter is usually taken to be zero or 5% of the disk mass. Using an iterative process from [Canup & Asphaug \(2001\)](#), the SPH particles are classified as either planet, disk, or escapees. The particles are assumed to undergo energy dissipation due to mutual particle collision leading to circular orbits. Planet particles have a semi-major axis that is less than the equatorial radius of the planet<sup>3</sup>. Escapees have enough kinetic energy to become gravitationally unbound, and the remaining particles are disk particles. The angular momentum of the planet and disk particles then gives the total angular momentum of the bound system ( $L_{sys}$ ). The fraction of iron particles in the disk determines the iron abundance of the resulting satellite ( $\delta_{FE}$ ). To clarify the subscript notation: the deviation in the isotopic composition of the resulting planet and satellite can be determined using a mass balance equation and the epsilon notation ([Canup 2012](#)):

$$\delta f_T = 100 \left( \frac{F_D}{F_P} - 1 \right), \quad (5)$$

where  $F_D$  and  $F_P$  are the mass fractions of silicate material from the target planet in the resulting disk and planet, respectively, and  $\delta f_T$  represents the percentage compositional deviation of the disk from the resulting planet, such that a  $\delta f_T = 0$  represents a disk with an equal fraction of target material as in the resulting planet. The required FeO/MgO ratios of proto-Earth and Theia can be determined using a similar method. A generalized expression can be developed for  $n$  materials with different compositions (Appendix C). In the case of the PEM model, we require two different proto-Earth materials, one solid and its respective melt. The FeO-to-MgO ratio for the Moon and the Earth becomes:

$$Q_M = 1 - \delta_P \left( \frac{\delta f_T}{100} (1 - Q_{tar,solid}) + Q_{tar,solid} \left( 1 - \frac{1}{K} \right) \delta_{enrich} \right) \quad (6)$$

$$Q_i = \frac{\Delta_i}{\Delta_E} \quad \Delta_i = \left( \frac{\text{FeO}}{\text{MgO}} \right)_i \quad \delta_{enrich} = \frac{F_{D,molten}}{\delta_P} - \delta_{P,molten} (1 - F_D)$$

$$\delta_P = \frac{F_P}{1 - F_P} \quad \delta_{P,molten} = \frac{F_{P,molten}}{F_P}.$$

<sup>2</sup> It can be greater than  $L_{EM}$  due to tidal interaction with the Sun. If the Moon was captured in evection resonance, the angular momentum could decrease by a factor of two ([Ćuk & Stewart 2012](#)).

<sup>3</sup> To give a good correlation with the equatorial radius of the fast-spinning case, the gyration constant is set to 0.69.

Here, subscript solid and molten represents the solid and molten silicate material, respectively,  $F_{P,molten}$  and  $F_{D,molten}$  are the mass fractions of molten material from the target planet in the resulting planet and disk,  $K$  is the exchange function with respect to the solid material (olivine),  $\delta_{enrich}$  estimates the effective enrichment of FeO/MgO in the resulting disk,  $\delta_{P,molten}$  describes how much of the resulting planet is composed of the molten part, and  $\delta_P$  describes how much target material versus impactor material ends up in the resulting planet. We can calculate  $Q_M$ ,  $\Delta_E$ ,  $\Delta_m$  from the FeO and MgO abundances on Earth and the Moon ([Warren 2005](#)):

$$\begin{aligned} \Delta_E &= 0.211 & (\text{FeO})_E &= 7.67\% & (\text{MgO})_E &= 36.4\% \\ \Delta_M &= 0.315 & (\text{FeO})_M &= 10.6\% & (\text{MgO})_M &= 33.7\% \\ Q_M &= 1.4927. \end{aligned}$$

The exchange function of olivine and its melt has its average at 0.35 ([Mibe et al. 2006](#)):

$$K = \frac{\Delta_{tar,solid}}{\Delta_{tar,molten}} = \frac{\left( \frac{\text{FeO}}{\text{MgO}} \right)_{olv,solid}}{\left( \frac{\text{FeO}}{\text{MgO}} \right)_{olv,molten}} = 0.35. \quad (7)$$

After a simulation we can calculate  $\delta_P$ ,  $\delta f_T$ , and  $\delta_{enrich}$ . Together with the value of  $Q_M$  we can calculate  $Q_{tar,solid}$  from Eq. (6). Concurrently this also gives  $Q_{imp}$ .

Before we continue to the simulation results, we investigate which collisions give satisfactory isotope and FeO/MgO ratios. The equations that are of interest in this analysis are as follows.

$$\delta_{enrich} = \frac{\frac{1-Q_M}{\delta_P} - \frac{\delta f_T}{100} (1 - Q_{tar,solid})}{Q_{tar,solid} \left( 1 - \frac{1}{K} \right)}, \quad (8)$$

$$Q_{imp} = 1 + \delta_P \left[ 1 - Q_{tar,solid} + \delta_{P,molten} Q_{tar,solid} \left( 1 - \frac{1}{K} \right) \right]. \quad (9)$$

Because of the isotopic similarity between the Earth and the Moon, the parameter  $\delta f_T$  is restricted depending on the isotopic composition of Theia. [Meier et al. \(2014\)](#) and [Herwartz et al. \(2014\)](#) give the required criterion parameter for  $\delta f_T$  for CI-chondrite, Angrite, Vesta, Mars, and Enstatite composition:

$$\begin{aligned} |\delta f_T| &< 6\% & \text{CI - chondrite, Angrite, Vesta, Mars} \\ |\delta f_T| &< 40\% & \text{Enstatite.} \end{aligned}$$

In [Canup \(2012\)](#), an upper value of the isotopic composition of Theia is taken to be one-eighth of Mars which then gives a criterion of:

$$|\delta f_T| < 13\%.$$

To further restrict our parameter space, we set a realistic maximum and minimum FeO/MgO ratio of our impactor. A realistic maximum FeO content would be around 30% ([Meier et al. 2014](#)), which would correspond to a FeO/MgO ratio of around unity. This then gives us  $Q_{imp,max} \approx 5$  (about double that of Mars:  $Q_{Mars} \approx 2.6$ ). The minimum is set to the limiting value of  $Q = 0$ . We choose three values of  $\delta_P$  to look at. High, intermediate, and low values are chosen to represent the different cases: Low  $\delta_P = 4$ , Intermediate  $\delta_P = 8$ , High  $\delta_P = 16$ . Finally we set a restriction on  $\delta_{P,molten}$ . We also choose three values here: one which represents the removal of all molten material from the planet  $\delta_{P,molten} = 0$ , an intermediate value of  $\delta_{P,molten} = 0.15$ , and

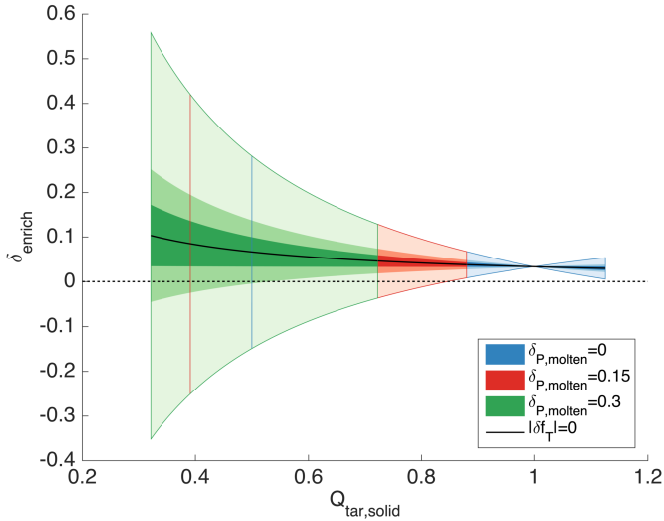


**Fig. 3.** Result of the compositional analysis with  $\delta_p = 8$ . The blue, red, and green areas represent the cases in which the ratios of molten material in the resulting planet are  $\delta_{P,\text{molten}} = 0, 0.15, 0.3$  respectively. The vertical red and blue lines represent the extent of the red and blue areas. The light colors represent  $|\delta f_T| < 40\%$ , medium colors represent  $|\delta f_T| < 13\%$ , and dark colors represent  $|\delta f_T| < 6\%$ . The black dashed line highlights  $\delta_{\text{enrich}} = 0$  and the black solid line highlights  $|\delta f_T| = 0$ .

a high value of  $\delta_{P,\text{molten}} = 0.3$ . Given  $Q_M$  and the partition function  $K$  together with all of the restrictions, we solve Eqs. (8) and (9) for a range of different  $Q_{\text{tar,solid}}$  values. The result of the analysis is plotted in Fig. 3 ( $\delta_p = 8$  and the rest is given in Appendix C). From this, we can see that the addition of a molten ocean opens up more possibilities in different compositions of Theia and proto-Earth. The parameters  $\delta_{\text{enrich}} = 0$  and  $\delta_{P,\text{molten}} = 0$  represents the classical Theia–Earth collision with only one target silicate material. We can see from Fig. 3 that the classical Theia–Earth collision is only possible for the enstatite composition case, requiring a  $Q_{\text{tar,solid}}$  close to unity and a high  $Q_{\text{imp}}$ . Increasing  $\delta_{P,\text{molten}}$  leads to a larger range in the  $\delta_{\text{enrich}}$  parameter, but restricts  $Q_{\text{tar,solid}}$  to smaller ranges and values. Another trend that can be seen is the effect of increasing  $\delta_p$ , which reduces the range of  $Q_{\text{tar,solid}}$  but decreases the required value of  $\delta_{\text{enrich}}$  for the smaller  $|\delta f_T|$  values. Figure 4 shows the allowed composition of the impactor for different kinds of  $\delta_p$ . As we can see, an increase in  $\delta_p$  narrows the range of possible  $Q_{\text{tar,solid}}$  values.

## 4. Simulation results

We divide the simulation results into two sections. The first outlines simulations done on a nonrotating proto-Earth, which we call the “canonical case” (denoted “c”). In the second section, called the “fast-spinning case” (denoted “f”) we outline simulations of a rapidly rotating proto-Earth with a period of 2.3 h  $\leftrightarrow$  3 h. We make use of the models and methods that we have described in the previous sections and investigate the effect of different impact parameters and planetary compositions on the resulting Moon. All the rendered figures in the upcoming sections were visualized using SPLASH (Price 2007).

### 4.1. Canonical case

We performed 65 simulations of the lunar-forming impact with a nonrotating proto-Earth with a mass of  $M_{\text{tar}} = 0.95M_E$  and an impactor with a mass of  $M_{\text{imp}} = 0.142M_E$ . A total of 12 simulations were run with the simple-layered proto-Earth

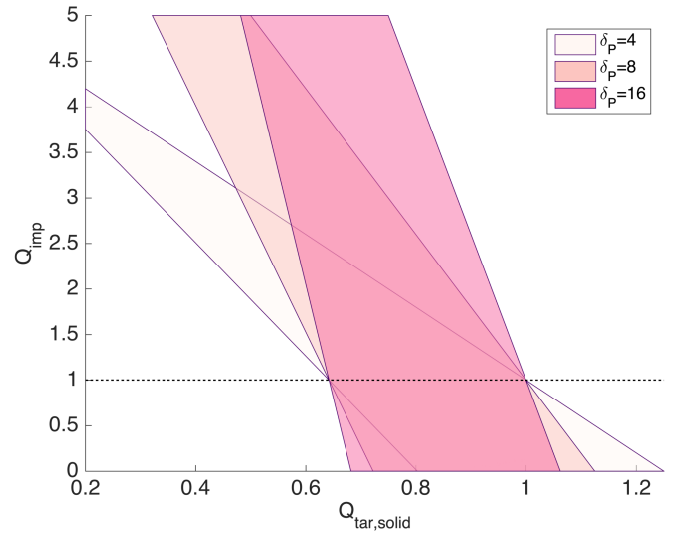


**Fig. 4.** Allowed values for the relative FeO/MgO of the target planet and impactor for different  $\delta_p$ . The boundary line to the right of each shaded area represents  $\delta_{P,\text{molten}} = 0$  and the boundary line to the left represents  $\delta_{P,\text{molten}} = 0.3$ .

model (Tables A.6, A.7) together with the rocky Theia model (Table A.9) at a high resolution of  $N = 3.3 \times 10^6$  particles (simulations referred to as  $Hrc\#_{\text{Solid/Molten}}$ ). A total of 53 simulations were run with the multi-layered proto-Earth model (Tables A.4, A.5) where 6 simulations were run with high resolution  $N = 3.3 \times 10^6$  particles (simulations referred to as  $Hrc\#_{\text{Solid/Molten}}$ ). One simulation was run with  $N = 1.2 \times 10^6$  particles ( $Mrc1_{\text{Solid}}$ ) to check convergence. Also, 46 simulations were done with low resolution  $N = 1.2 \times 10^5$  particles, 30 of which were run with the rocky Theia model (simulations referred to as  $Lrc\#_{\text{Solid/Molten}}$ ) and the rest with the icy Theia model (Table A.10), these simulations are denoted as  $Lic\#_{\text{Solid/Molten}}$ . For each simulation, the impact angle and angular momentum of the impact was varied. Each of the simulations ran for 24 h and their results can be seen in Table 1.

In Figs. 5–10 we show the evolution of the high-resolution case: “ $Hrc1_{\text{Solid}}$ ”. In this case, the proto-Earth is modeled using the multi-layered PES model together with a rocky Theia. Figure 5 shows the pre-impact conditions from an equatorial view and a top-down view. The color rendering shows the temperature of each SPH particle. The impact parameter and angular momentum are in this case set to  $b = 0.3$  and  $L_i = 1.25L_{\text{EM}}$  respectively. In Fig. 6 we see the state of the simulation in the top-down view at different times ( $t = 0.25, 1, 2, 5, 7.5, 15$ h). The impactor can be seen hitting in an oblique angle which results in shearing of the impactor. The impact leads to the formation of a pressure wave bulge that starts to go around the planet, a stream of infalling material follows right behind, heating the planet. At around  $t = 2$ h, the wave bulge starts to collapse into the planet which releases a large amount of heat energy. At  $t = 5$ h, the planet is rotating rapidly and the sheared-off material has developed into a stream that extends out from the planet. In the stream, we can see several satellites have started to form, especially the large satellite seen in the bottom left of  $t = 5$ h which has approximately the mass of the Moon. The collapse of the initial wave bulge forms another pressure wave that goes around the planet. This pressure wave hits the tidal stream at  $t = 5$ h which creates a strong torque on the infalling stream, and together with the high outward pressure from the heated vaporized surface, the stream is pushed into a larger orbit, which can be seen in  $t = 7.5$ h. After

**Table 1.** System properties of the canonical impact simulations.

Simulations run as in the canonical case using the rocky Theia model												
Run	$b$	$\frac{L_{\text{imp}}}{L_{\text{EM}}}$	$\frac{L_{\text{sys}}}{L_{\text{EM}}}$	$\frac{L_D}{L_{\text{EM}}}$	$\frac{M_D}{M_M}$	$\delta_{\text{FE}}[\%]$	$\frac{M_{\text{esc}}}{M_M}$	$\delta f_T[\%]$	$\delta_{\text{enrich}}$	$Q_{\text{tar,solid}}$	$Q_{\text{imp}}$	$\frac{M_m}{M_M}$
<i>Hrc1</i> <sub>Solid</sub>	0.73	1.26	1.23	0.34	2.22	5	0.31	-52	0.00	0.88	1.95	1.19
<i>Hrc1</i> <sub>Molten</sub>	0.73	1.26	1.22	0.30	1.99	5	0.32	-46	-0.02	0.78	1.45	0.98
<i>Hrc2</i> <sub>Solid</sub>	0.70	1.26	1.21	0.37	2.38	5	0.42	-59	0.00	0.90	1.83	1.29
<i>Hrc2</i> <sub>Molten</sub>	0.70	1.26	1.21	0.33	2.09	5	0.44	-56	-0.04	0.78	1.45	1.18
<i>Hrc3</i> <sub>Solid</sub>	0.67	1.26	1.04	0.20	1.36	8	1.59	-43	0.00	0.86	2.15	0.57
<i>Hrc3</i> <sub>Molten</sub>	0.67	1.26	1.02	0.16	1.17	6	1.67	-37	-0.01	0.78	1.51	0.41
<i>Mrc1</i> <sub>Solid</sub>	0.73	1.26	1.23	0.37	2.42	5	0.26	-57	0.00	0.89	1.86	1.23
<i>Lrc1</i> <sub>Solid</sub>	0.73	1.26	1.19	0.32	2.15	3	0.48	-50	0.00	0.88	1.98	1.04
<i>Lrc1</i> <sub>Molten</sub>	0.73	1.26	1.18	0.31	1.97	2	0.53	-52	-0.04	0.77	1.50	1.08
<i>Lrc2</i> <sub>Solid</sub>	0.70	1.26	1.14	0.31	2.06	3	0.80	-60	0.00	0.90	1.82	0.99
<i>Lrc2</i> <sub>Molten</sub>	0.70	1.26	1.12	0.27	1.79	2	0.94	-51	-0.04	0.78	1.50	0.84
<i>Lrc3</i> <sub>Solid</sub>	0.67	1.26	1.02	0.19	1.29	4	1.66	-41	0.00	0.86	2.21	0.54
<i>Lrc3</i> <sub>Molten</sub>	0.67	1.26	1.07	0.21	1.45	4	1.29	-49	-0.04	0.77	1.54	0.60
<i>Lrc4</i> <sub>Solid</sub>	0.50	1.26	0.87	0.09	0.66	10	2.84	-39	0.00	0.85	2.27	0.24
<i>Lrc4</i> <sub>Molten</sub>	0.50	1.26	0.87	0.10	0.69	8	2.95	-38	-0.03	0.74	1.95	0.27
<i>Lrc5</i> <sub>Solid</sub>	0.70	1.36	1.09	0.30	1.77	4	1.82	-52	0.00	0.90	1.95	1.22
<i>Lrc5</i> <sub>Molten</sub>	0.70	1.36	1.12	0.31	1.81	8	1.60	-51	-0.04	0.77	1.56	1.24
<i>Lrc6</i> <sub>Solid</sub>	0.70	1.16	1.12	0.25	1.84	1	0.31	-63	0.00	0.90	1.79	0.65
<i>Lrc6</i> <sub>Molten</sub>	0.70	1.16	1.10	0.18	1.32	2	0.46	-52	-0.04	0.77	1.50	0.50
<i>Lrc7</i> <sub>Solid</sub>	0.30	1.26	0.56	0.17	1.42	14	8.34	-20	0.00	0.74	3.50	0.26
<i>Lrc7</i> <sub>Molten</sub>	0.30	1.26	0.57	0.20	1.43	18	8.17	-16	-0.01	0.58	3.89	0.53
<i>Lrc8</i> <sub>Solid</sub>	0.50	1.36	0.84	0.11	0.72	13	3.73	-41	0.00	0.87	2.21	0.40
<i>Lrc8</i> <sub>Molten</sub>	0.50	1.36	0.84	0.16	1.01	17	3.79	-48	-0.04	0.76	1.82	0.55
<i>Lrc9</i> <sub>Solid</sub>	0.80	1.26	1.24	0.39	2.33	1	0.12	-63	0.00	0.90	1.78	1.51
<i>Lrc9</i> <sub>Molten</sub>	0.80	1.26	1.24	0.39	2.32	1	0.13	-56	-0.04	0.78	1.46	1.51
<i>Lrc10</i> <sub>Solid</sub>	0.80	1.36	1.32	0.43	2.60	7	0.30	-59	0.00	0.90	1.83	1.69
<i>Lrc10</i> <sub>Molten</sub>	0.80	1.36	1.31	0.44	2.59	10	0.32	-52	-0.04	0.78	1.42	1.73
<i>Lrc11</i> <sub>Solid</sub>	0.50	1.51	0.74	0.20	1.23	23	5.28	-47	0.00	0.90	2.05	0.80
<i>Lrc11</i> <sub>Molten</sub>	0.50	1.51	0.73	0.19	1.12	25	5.42	-44	-0.04	0.76	1.90	0.77
<i>Lrc12</i> <sub>Solid</sub>	0.30	1.36	0.45	0.43	2.66	30	11.02	-24	0.00	0.81	3.06	1.64
<i>Lrc12</i> <sub>Molten</sub>	0.30	1.36	0.45	0.47	2.66	35	10.92	-25	-0.02	0.71	2.68	1.99
<i>Lrc13</i> <sub>Solid</sub>	0.40	1.26	0.76	0.07	0.60	10	4.30	-25	0.00	0.78	2.98	0.11
<i>Lrc13</i> <sub>Molten</sub>	0.40	1.26	0.77	0.08	0.64	7	4.20	-21	-0.01	0.66	2.87	0.17
<i>Lrc14</i> <sub>Solid</sub>	0.60	1.26	0.96	0.12	0.90	5	2.06	-42	0.00	0.86	2.18	0.28
<i>Lrc14</i> <sub>Molten</sub>	0.60	1.26	0.97	0.13	0.94	4	2.05	-42	-0.03	0.76	1.69	0.33
<i>Lrc15</i> <sub>Solid</sub>	0.76	1.26	1.22	0.35	2.11	2	0.28	-59	0.00	0.89	1.84	1.35
<i>Lrc15</i> <sub>Molten</sub>	0.76	1.26	1.22	0.35	2.23	1	0.29	-54	-0.04	0.78	1.46	1.27
Simulations run as in the canonical case using the simple-layered proto-Earth model												
Run	$b$	$\frac{L_{\text{imp}}}{L_{\text{EM}}}$	$\frac{L_{\text{sys}}}{L_{\text{EM}}}$	$\frac{L_D}{L_{\text{EM}}}$	$\frac{M_D}{M_M}$	$\delta_{\text{FE}}[\%]$	$\frac{M_{\text{esc}}}{M_M}$	$\delta f_T[\%]$	$\delta_{\text{enrich}}$	$Q_{\text{tar,solid}}$	$Q_{\text{imp}}$	$\frac{M_m}{M_M}$
<i>Hdrc1</i> <sub>Solid</sub>	0.73	1.26	1.23	0.16	0.97	5	0.25	-42	0.00	0.83	2.16	0.58
<i>Hdrc1</i> <sub>Molten</sub>	0.73	1.26	1.22	0.16	1.12	4	0.31	-24	0.03	0.87	0.19	0.45
<i>Hdrc2</i> <sub>Solid</sub>	0.73	1.34	1.30	0.41	2.55	4	0.31	-64	0.00	0.91	1.77	1.53
<i>Hdrc2</i> <sub>Molten</sub>	0.73	1.34	1.30	0.43	2.69	4	0.32	-59	-0.06	0.75	1.33	1.58
<i>Hdrc3</i> <sub>Solid</sub>	0.73	1.43	1.31	0.51	2.8	6	0.71	-62	0.00	0.91	1.8	2.27

**Notes.** Hdrc# are high-resolution simulations run with the simple-layered proto-Earth model. The simulations run with the multi-layered proto-Earth are Hrc# which is run with  $N = 3.3 \times 10^6$  particles and *Mrc1*<sub>solid</sub> which is a simulation run with  $N = 1.2 \times 10^6$  particles and the rest of the simulations were run with  $N = 1.2 \times 10^5$  particles. rc# indicates simulations run with a rocky impactor and ic# indicates simulations run with an icy impactor. Here,  $b$  is the impact parameter,  $L_{\text{imp}}$  is the angular momentum of the impact,  $L_{\text{sys}}$  is the angular momentum of the bound system,  $L_D$  is the angular momentum of the disk,  $M_D$  is the disk mass,  $\delta_{\text{FE}}$  is the iron content of the disk,  $M_{\text{esc}}$  escaping mass, and  $M_m$  is the estimated mass of the satellite. The parameters are scaled by the angular momentum of the Earth–Moon system ( $L_{\text{EM}}$ ) and by the mass of the Moon ( $M_M$ ). The compositional parameters ( $\delta f_T$ ,  $\delta_{\text{enrich}}$ ,  $Q_{\text{imp}}$ ,  $Q_{\text{tar,solid}}$ ) are all defined in Sect. 3.

Table 1. continued.

Simulations run as in the canonical case using the simple-layered proto-Earth model												
Run	$b$	$\frac{L_{\text{imp}}}{L_{\text{EM}}}$	$\frac{L_{\text{sys}}}{L_{\text{EM}}}$	$\frac{L_D}{L_{\text{EM}}}$	$\frac{M_D}{M_M}$	$\delta_{\text{FE}}[\%]$	$\frac{M_{\text{esc}}}{M_M}$	$\delta_{f_T}[\%]$	$\delta_{\text{enrich}}$	$Q_{\text{tar,solid}}$	$Q_{\text{imp}}$	$\frac{M_m}{M_M}$
<i>Hdrc3</i> <sub>Molten</sub>	0.73	1.43	1.12	0.27	1.52	5	2.00	-47	-0.04	0.75	1.32	1.19
<i>Hdrc4</i> <sub>Solid</sub>	0.70	1.26	1.22	0.3	2.09	3	0.39	-62	0.00	0.90	1.80	0.87
<i>Hdrc4</i> <sub>Molten</sub>	0.70	1.26	1.21	0.26	1.78	2	0.47	-61	-0.07	0.73	1.43	0.81
<i>Hdrc5</i> <sub>Solid</sub>	0.70	1.37	1.07	0.20	1.21	9	2.02	-44	0.00	0.87	2.12	0.82
<i>Hdrc5</i> <sub>Molten</sub>	0.70	1.37	1.07	0.20	1.22	9	2.07	-35	-0.02	0.76	1.17	0.78
<i>Hdrc6</i> <sub>Solid</sub>	0.67	1.26	1.04	0.12	0.84	5	1.66	-39	0.00	0.84	2.25	0.31
<i>Hdrc6</i> <sub>Molten</sub>	0.67	1.26	1.02	0.08	0.62	3	1.74	-37	-0.03	0.73	1.47	0.20
Simulations run as in the canonical case using the icy Theia model												
Run	$b$	$\frac{L_{\text{imp}}}{L_{\text{EM}}}$	$\frac{L_{\text{sys}}}{L_{\text{EM}}}$	$\frac{L_D}{L_{\text{EM}}}$	$\frac{M_D}{M_M}$	$\delta_{\text{FE}}[\%]$	$\frac{M_{\text{esc}}}{M_M}$	$\delta_{f_T}[\%]$	$\delta_{\text{enrich}}$	$Q_{\text{tar,solid}}$	$Q_{\text{imp}}$	$\frac{M_m}{M_M}$
<i>Lic1</i> <sub>Solid</sub>	0.73	1.28	1.20	0.51	2.77	0	0.56	-88	0.00	0.91	1.56	2.28
<i>Lic1</i> <sub>Molten</sub>	0.73	1.28	1.22	0.50	2.78	0	0.50	-81	-0.07	0.77	1.39	2.21
<i>Lic2</i> <sub>Solid</sub>	0.73	1.38	1.33	0.90	5.84	0	0.43	-92	0.00	0.94	1.54	3.12
<i>Lic2</i> <sub>Molten</sub>	0.73	1.38	1.32	0.88	5.95	0	0.45	-91	-0.10	0.78	1.46	2.78
<i>Lic3</i> <sub>Solid</sub>	0.80	1.28	1.21	0.52	2.76	0	0.33	-87	0.00	0.90	1.57	2.49
<i>Lic3</i> <sub>Molten</sub>	0.80	1.28	1.26	0.53	2.90	0	0.21	-79	-0.07	0.77	1.38	2.39
<i>Lic4</i> <sub>Solid</sub>	0.50	1.28	0.59	0.14	0.82	0	4.45	-74	0.00	0.91	1.66	0.58
<i>Lic4</i> <sub>Molten</sub>	0.50	1.28	0.54	0.09	0.56	0	5.09	-76	-0.07	0.78	1.47	0.34
<i>Lic5</i> <sub>Solid</sub>	0.50	1.38	0.53	0.14	0.84	0	5.44	-77	0.00	0.92	1.64	0.55
<i>Lic5</i> <sub>Molten</sub>	0.50	1.38	0.52	0.14	0.79	0	5.69	-75	-0.07	0.79	1.45	0.60
<i>Lic6</i> <sub>Solid</sub>	0.67	1.28	1.17	0.67	4.13	0	0.80	-89	0.00	0.93	1.55	2.56
<i>Lic6</i> <sub>Molten</sub>	0.67	1.28	1.16	0.64	3.94	0	0.87	-91	-0.10	0.77	1.45	2.41
<i>Lic7</i> <sub>Solid</sub>	0.30	1.28	0.31	0.12	1.02	0	9.07	-42	0.00	0.88	2.17	0.11
<i>Lic7</i> <sub>Molten</sub>	0.30	1.28	0.28	0.11	0.95	0	9.03	-41	-0.02	0.79	1.74	0.14
<i>Lic8</i> <sub>Solid</sub>	0.60	1.28	0.74	0.25	1.42	0	3.28	-83	0.00	0.92	1.59	1.08
<i>Lic8</i> <sub>Molten</sub>	0.60	1.28	0.60	0.09	0.67	0	4.33	-77	-0.08	0.77	1.45	0.25

$t = 12$  h, the large satellite is on a course to recollide with the planet. This eventually shears off some additional material into orbit which can be seen in Fig. 7, where the state of the system after  $t = 24$  h is presented. The temperature profile of the inner  $r < 1R_e$  is plotted in Fig. 10 before and after impact (for both the multi-layered case and the simple-layered case). The planet with its extended vaporized atmosphere has temperatures in the range of  $3 \times 10^3 \leftrightarrow 3 \times 10^4$  K with an average temperature of  $T_{\text{avg}} = 5604$  K.

Figure 8 shows a color rendering of the density at the end of the simulation from a top-down view and an equatorial view. We can see a disk-like structure around an almost spherical inner planet. Several small satellites can be seen in the extending material stream. Figure 9 shows the distribution of iron and silicate at the end of the simulation. This figure also shows the result from our disk analysis. Assuming no mass loss from the subsequent disk evolution, we get an estimated Moon mass of  $M_m = 1.19M_M$ , and with a mass loss of around 5% in the disk evolution we get an estimated Moon mass of  $M_m = 1.02M_M$ . The stream of particles that extends out from the planet mostly consists of impactor material. This is reasonable as the material comes mostly from the larger satellite, which was formed early on from the sheared-off impactor material that collided late in the simulation. The composition of the disk is dominated by impactor material with  $\delta_{f_T} = -52\%$ ; the iron content is below 10% and the estimated relative FeO/MgO ratio of the impactor and target is  $Q_{\text{tar,solid}} = 0.88$ ,  $Q_{\text{imp}} = 1.95$ . The high  $\delta_{f_T}$  requires

an impactor that has near-identical isotopic ratios to that of Earth. The iron content and the  $Q$  ratio are however well within the acceptable ranges. The angular momentum of the bounded system is slightly higher than the Earth–Moon system, namely  $L_{\text{sys}} = 1.23L_{\text{EM}}$ .

Figure 11 shows the impact properties of all the simulations from Table 1. A description of each symbol, color, and size is given in the caption. In Fig. 11a we can see a linear relationship between the disk mass and its angular momentum. Fitting the *Lrc#* data to a polynomial we find  $L_D = 0.1745M_D$ . Rewriting Eq. (4) in terms of  $L_e m$  and  $M_m$  and inserting the relationship into the equation we get  $M_m \approx 0.74M_D$ . Fitting to the *Hdrc#* data and we get  $L_D = 0.1733M_D$  and  $M_m \approx 0.73M_D$  and fitting to the *Lic#* data we get  $L_D = 0.1575M_D$  and  $M_m \approx 0.56M_D$ .

#### 4.2. Fast-spinning case

We performed 28 simulations of the Moon-forming impact with a fast-rotating proto-Earth with a mass of  $M_{\text{tar}} = 1.05M_E$  and an impactor with a mass of  $M_{\text{imp}} = 0.05M_E$ . All simulations used about  $N = 3.1 \times 10^5$  SPH particles. The proto-Earth was in each case modeled using the multi-layered PES or PEM model described in Sect. 2.1 (Tables A.1 and A.2). These simulations are denoted *Lrf#*<sub>Solid/Molten</sub>. For six simulations, we used a simpler, two-layered model of a proto-Earth (Table A.3). These simulations are denoted *Lrdf#*<sub>Solid/Molten</sub>. Additionally, an extra

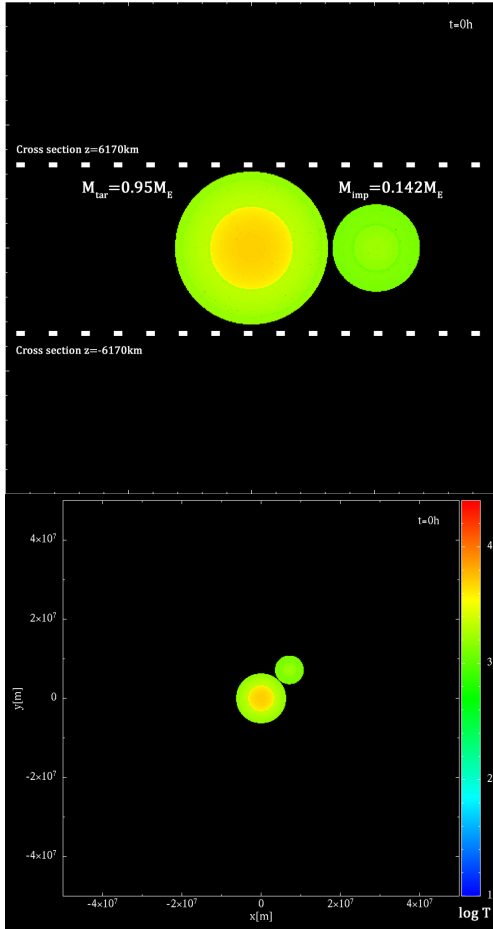


**Fig. 5.** Initial setup of the *Hrc1Solid* simulation. The impact parameter and angular momentum are in this case set to  $b = 0.3$  and  $L_{\text{imp}} = 1.25L_{\text{EM}}$  respectively. The color rendering represents the temperature. *Upper figure:* equatorial view of the initial setup. The cross section that can be seen represents the region in which particles are rendered, which is done to improve the clarity of the following figures. *Lower panel:* top-down view of the initial setup and is the viewpoint in the following figures.

two-layered model was made which was the same as the regular two-layered model but with material that had three times the vaporization energy. This simulation is denoted *Lrdf1Solid*<sup>x3</sup>. All the simulations used a rocky planetary model for Theia (Table A.8). For each simulation the impact angle, impact velocity, and rotation of the target planet were varied. The simulations ran for 24 h and their results can be seen in Table 2.

In Figs. 12–17 we show the evolution of the fast-spinning case of “*Lrf12Molten*”. In this case, the proto-Earth is modeled using the multi-layered PEM model. Figure 12 shows the pre-impact conditions from an equatorial view and a top-down view. From the very oblate target planet, we can see that the planet is spinning very rapidly. The color rendering shows the temperature of each SPH particle, and the color–temperature range can be seen in Fig. 12. The spin period, impact velocity, and angular momentum are set to  $P = 2.3$  h,  $b = -0.3$ , and  $v_{\text{imp}} = 20$  km s<sup>−1</sup> respectively. These starting values are taken from simulations done by Čuk & Stewart (2012). Figure 13 shows the state of the simulation in the top-down view at different times ( $t = 0.25, 1, 2, 5, 7.5, 12$  h). The impactor can be seen hitting the target head-on, which creates a strong shock-wave that propagates through the planet. Much of the impactor is swallowed by the target planet; however, there is also a significant amount that is scattered in the

$z$ -direction (which can better be seen from Fig. 17). As the planet falls in on itself due to its rapid rotation, it creates a torque and starts to fling material out into orbit. Similar to the canonical case we have a tidal bump that goes around the planet (albeit much smaller). After about 12 h the post-impact has calmed down, and we are left with a very hot planet and atmosphere. The average temperature of the planet and atmosphere is  $T_{\text{avg}} = 7700$  K, which is a significant increase compared to the canonical model. In these kinds of simulations, we are not left with any distinct stream of particles; instead we have a more isotropic distribution around the planet (see Fig. 14).

Figure 16 shows the distribution of iron and silicate content of the target and impactor material. This figure also shows the result from our disk analysis. Assuming no mass loss from the disk, we get an estimated Moon mass of  $M_m = 0.13M_M$ . We can also see that this type of simulation has a much more even distribution of the target and impactor material, leading to a lower  $\delta f_T = -8\%$ . The iron content in the disk is below 10% and the estimated FeO/MgO of the impactor and target is  $Q_{\text{tar,solid}} = 0.3$ ,  $Q_{\text{imp}} = 6.09$ . The angular momentum of the bounded system is much higher than the Earth–Moon system  $L_{\text{sys}} = 2.68L_{\text{EM}}$ . However, most of this comes from the planet and only  $L_D = 0.06L_{\text{EM}}$  is in the disk.

This type of collision has been seen to produce Moon-like satellites by Čuk & Stewart (2012); Nakajima & Stevenson (2014), but none of our simulations show this (see Fig. 18). To figure out the reason for this discrepancy, we performed several different tests. First we made a simpler model of the proto-Earth using only two layers, which is similar to the one used by Čuk & Stewart (2012). We find however that this does not significantly change the result ( $\Delta M_m \approx 0.02M_M$  between the *Lrf12Solid* and *Lrdf1Solid* case). We see a small increase in the mass of the disk ( $\Delta M_D \approx 0.07M_M$ ) and less mass escapes ( $\Delta M_{\text{esc}} \approx -0.43M_M$ ), but about the same angular momentum resides in the disk ( $L_D = 0.09L_{\text{EM}}$ ). This model does not therefore fix the discrepancy between the results. Next, we increased the vaporization energy of our silicate material to see if this had any effect. This also does not change the result significantly ( $\Delta M_m \approx 0.03M_M$  between the *Lrdf1Solid* and *Lrdf1Solid*<sup>x3</sup> case). We see a further increase in the disk mass ( $\Delta M_D \approx 0.08M_M$ ) and even less mass escapes the system ( $\Delta M_{\text{esc}} \approx -0.43M_M$ ). We also see a small increase in the disk angular momentum ( $\Delta L_D = 0.02L_{\text{EM}}$ ).

Figure 18 shows the impact properties of all the simulations in Table 2. A description of each symbol, color, and size is given in the caption. In Fig. 18a we can see a linear relationship between the disk mass and its angular momentum. Fitting the data to a polynomial we find  $L_D = 0.1327M_D$ . By inserting this value into Eq. (4), we obtain  $M_m \approx 0.3M_D$ .

## 5. Discussion

From the compositional analysis in Sect. 3 we saw that the classical Earth–Theia collision could only be satisfied for higher fractions of impactor material within the disk ( $\delta f_T < -40\%$ ), which would require an almost Earth-like isotopic composition for Theia. An enstatite composition for Theia is still possible, but all known samples have little to no FeO content which means that substantial oxidation of the lunar mantle would be required post-impact (Meier et al. 2014). This could be resolved if Theia was massive enough to incorporate a substantial amount of Si within its core, which would contribute to the oxidation of the mantle (Javoy 1995). A smaller  $|\delta f_T|$  allows for a larger difference in

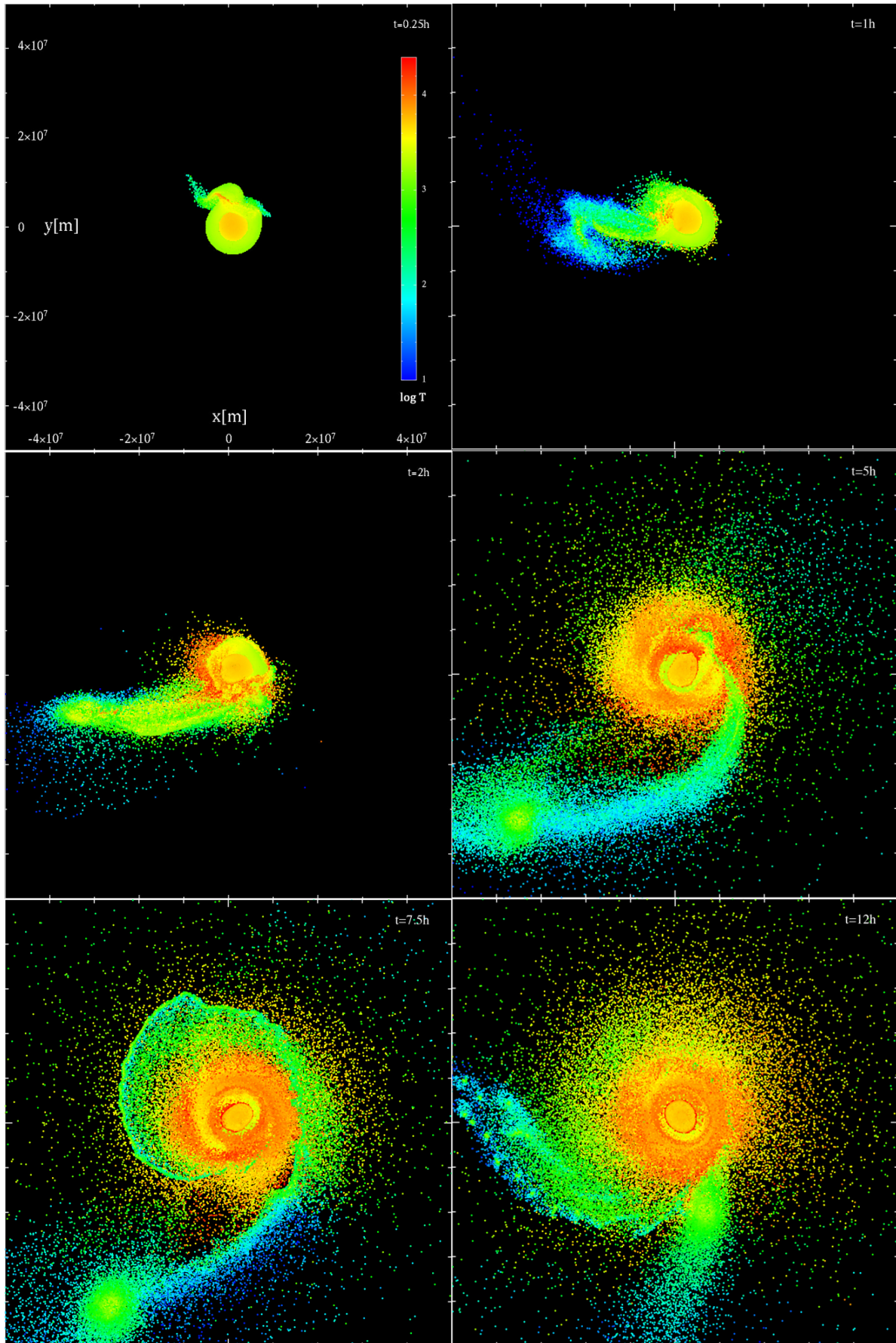


**Fig. 6.** Top-down view of the evolution of the collision for the  $Hrc1_{\text{Solid}}$  simulation. The temperature range and spatial range can be seen in the *top left figure*. The times when each of the images were captured, starting from the upper left, are  $t=0.25, 1, 2, 5, 7.5, 12\text{ h}$ .

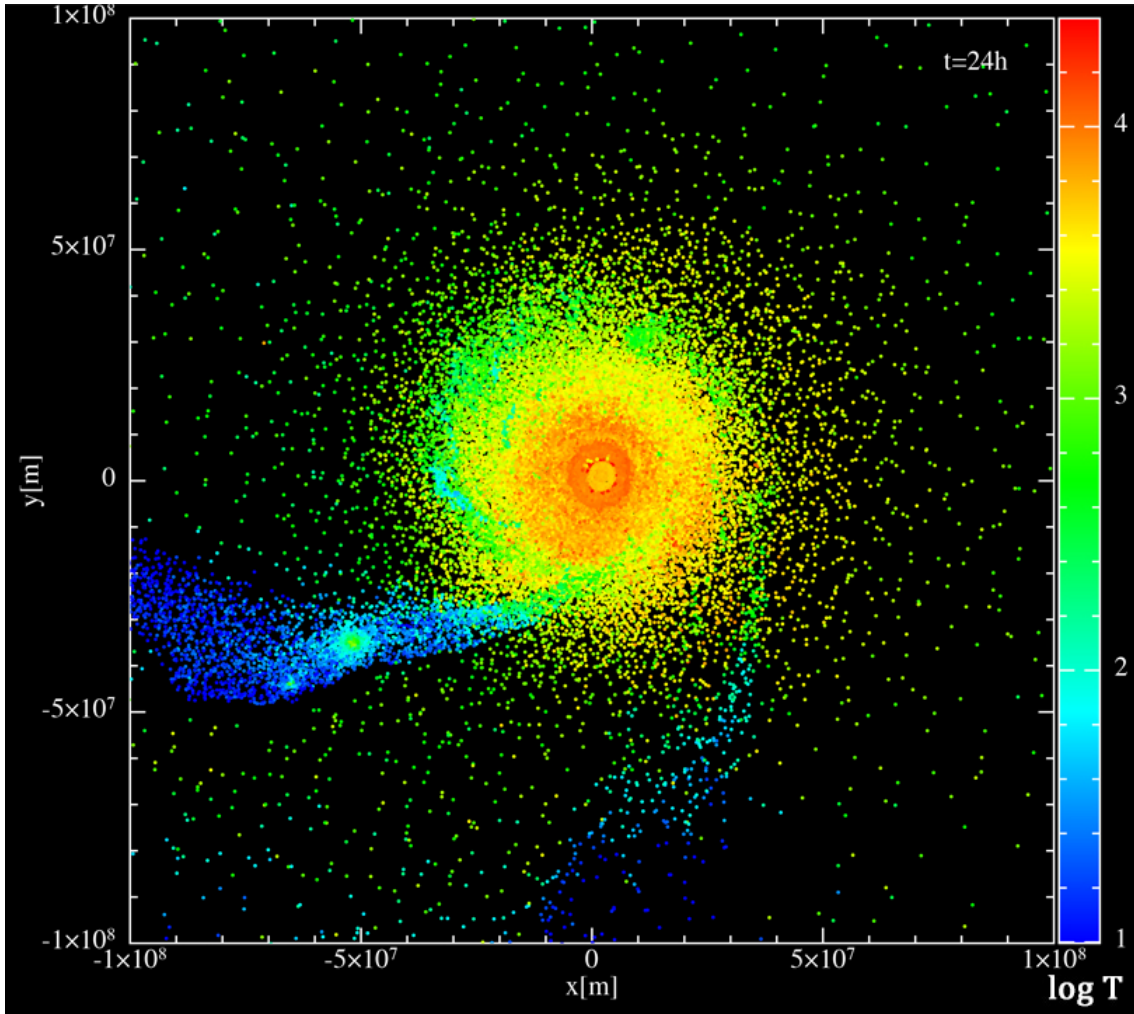


Fig. 7. State of the system after 24 h of simulation time.

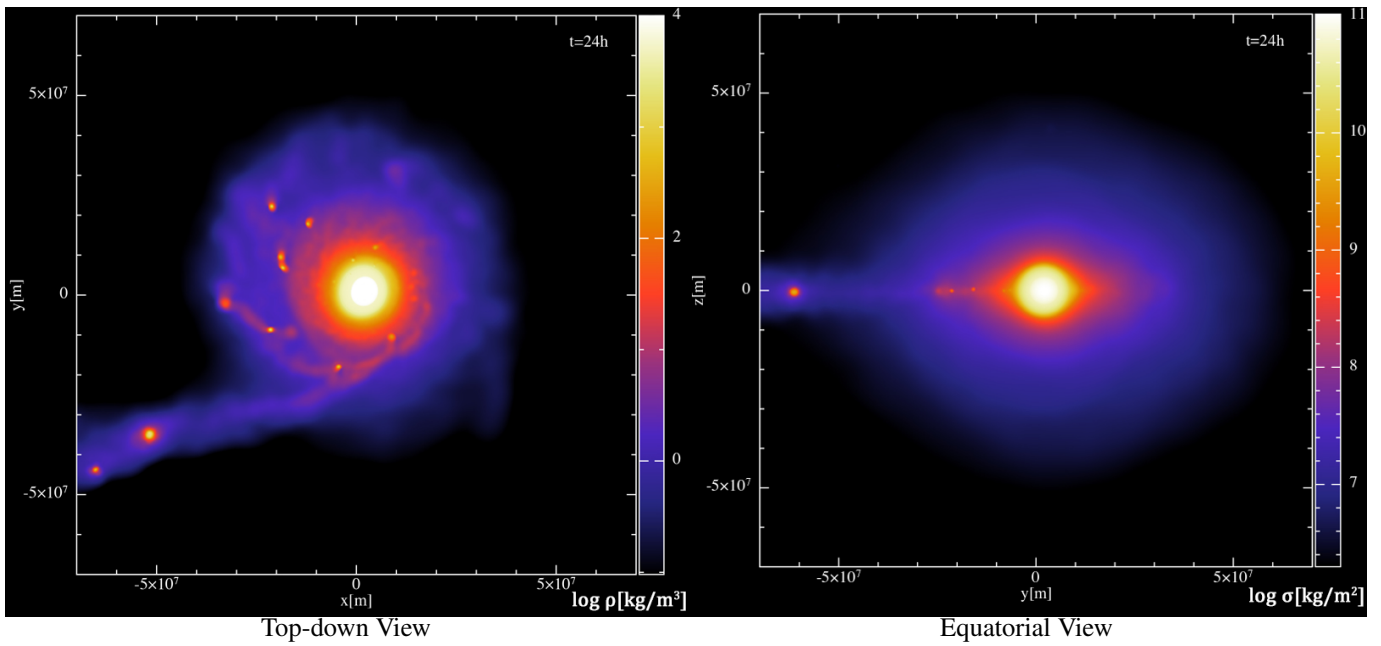
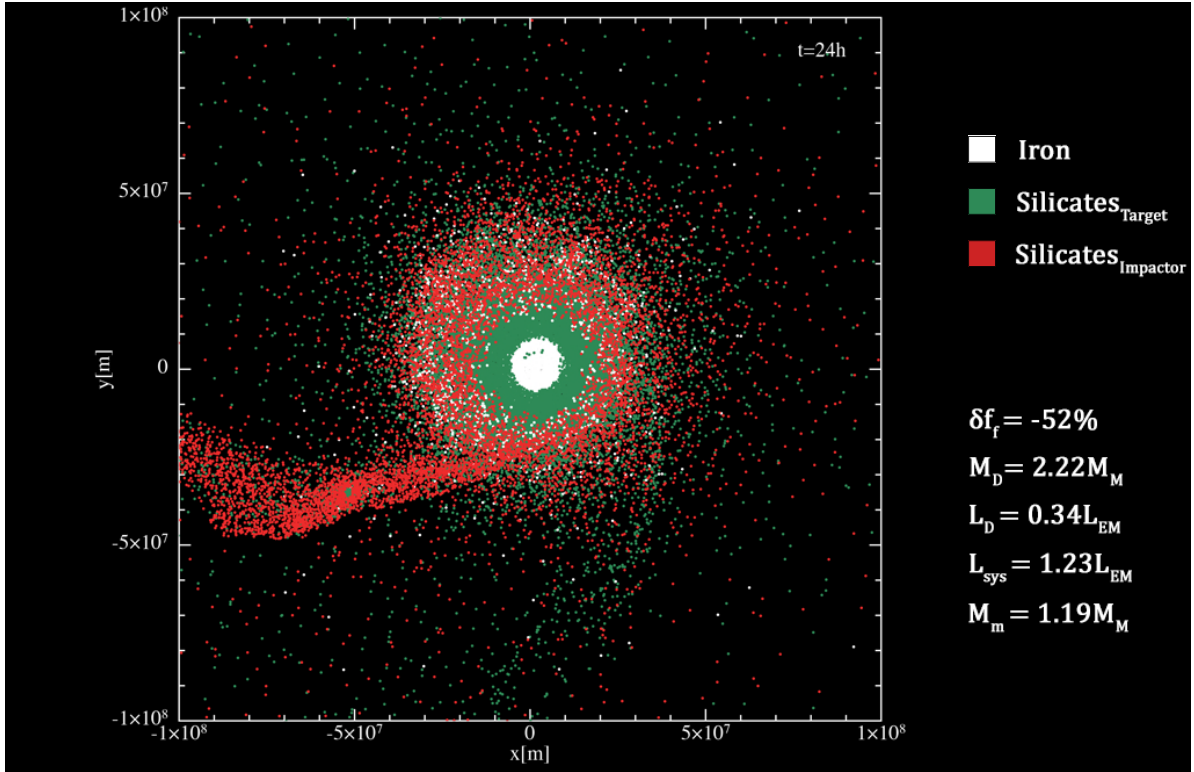
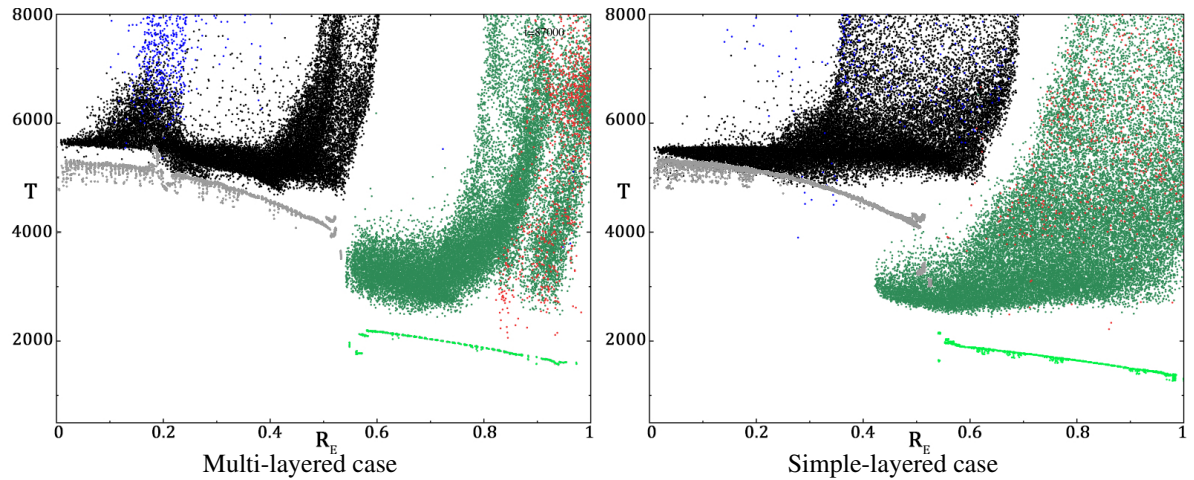


Fig. 8. Density rendering of the system after 24 h of simulation time. A disk-like structure can be seen around an almost spherical inner planet. The color rendering on the *right-hand picture* represents the column density.



**Fig. 9.** Compositional analysis after 24 h of simulation time. Colors denote the different materials and origins. We can see a stream of material that is dominated by impactor material. Assuming no mass loss from the subsequent disk evolution we get an estimated Moon mass of  $M_m = 1.23M_M$ .



**Fig. 10.** Temperature profile of the multi-layered proto-Earth (*left*) and simple-layered proto-Earth (*right*) before and 24 h after impact. The gray (core) and light green (mantle) show the pre-impact proto-earth conditions. The black (iron) and dark green (silicate) show material from the target planet, while blue (iron) and red (silicate) show material from the impactor. This can be directly compared to the figure from [Canup \(2008b\)](#) which looks at the same ranges. Comparing to their results we can see that both of our pre-impact proto-Earths have a more continuous temperature profile (except at core mantle boundary). The silicate mantle is around the same temperature while our iron core is about 1000–2000K hotter. The most significant difference can be seen in the multi-layered case, where in the post-impact results there is significant mixing between the outer core material and impactor core, which is not present in the simple-layered case or in the work of [Canup \(2008b\)](#). This is due to the outer core being in a hotter state (molten) as the impactor core slams into it, which causes an increase in the temperature of the outer core material as the impactor material mixes with it. The temperature of the shocked impactor material reaches around 34 000 K at its peak for the multi-layered case and about 42 000 K in the simple-layered case.

isotopic composition, but would require additional enrichment of FeO. The effective enrichment of the lunar mantle from the molten ocean is captured by the derived  $\delta_{\text{enrich}}$  parameter, in which a higher value would also allow for a smaller  $|\delta f_T|$ .

From our canonical simulation we find that all the simulations have reasonable  $Q_{\text{tar,solid}}$  values (Fig. 11d), however

$\delta f_T < -40\%$  for all viable Moon-forming impacts (Fig. 11c). We also see no effective enrichment of FeO in the lunar mantle for these simulations ( $\delta_{\text{enrich}} < 0.0$ ). This is because only a small fraction of the resulting disk is composed of the enriched molten material. In the high-resolution case, the effect of a molten ocean does in general result in a smaller Moon mass because of the

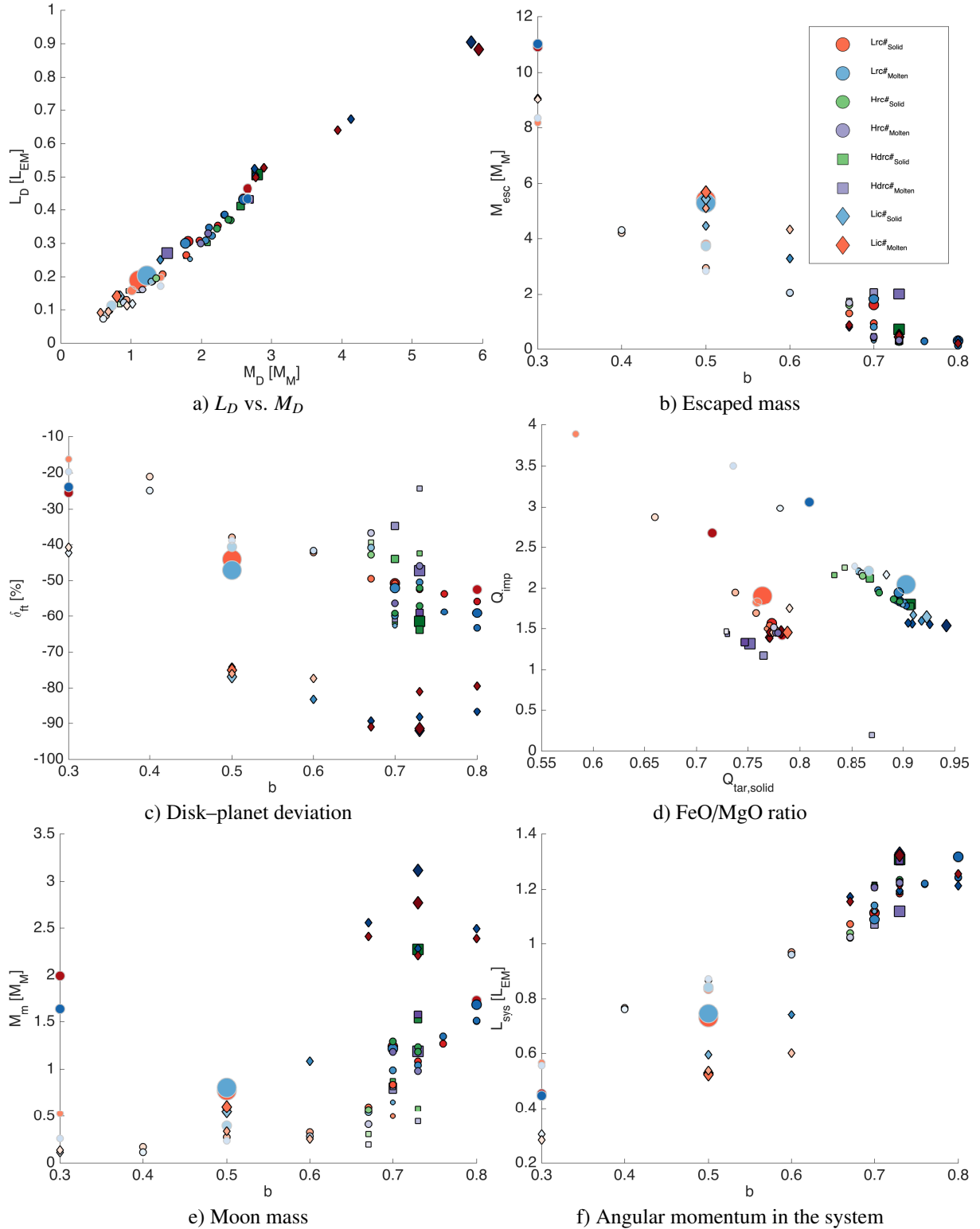


**Fig. 11.** Simulation results (those from Table 1). The size of the symbols represents the angular momentum of the impact. The colors represent different resolutions and whether the PES or PEM model were used: the blue and red represent the low-resolution PES and PEM models, while the green and purple represent the high-resolution PES and PEM model. The gradient in color represents the estimated mass of the Moon relative to the distribution. Surrounding gray borders represent cases that have more than 10% iron in their disk. Circles represent collisions made with a multi-layered proto-Earth and a rocky impactor, diamonds represent collisions made with a multi-layered proto-Earth and an icy impactor, and squares represent collisions made with a simple-layered proto-Earth and a rocky impactor. *Panel a*: linear relationship between the mass and angular momentum of the disk. *Panel b*: increase in escaped mass as the impact parameter decreases, which is because of the higher impact velocity required to recreate the given  $L_{imp}$ . From *panel c* we can see, in general, a high negative disk-planet deviation as we increase the impact parameter. *Panel d*: shows that  $Q$  values for all the simulations are within the realistic limits ( $0 < Q_{imp} < 5$ ). *Panels e and f*: show that most prominent impacts occur in the range of  $0.7 < b < 0.76$ .

**Table 2.** System properties of the fast-spinning simulations.

Simulations run as in the fast-spinning case using the regular proto-Earth model													
Run	$b$	$v_{\text{imp}}$	$P_{\text{tar}}$	$\frac{L_{\text{sys}}}{L_{\text{EM}}}$	$\frac{L_D}{L_{\text{EM}}}$	$\frac{M_D}{M_M}$	$\delta_{\text{FE}}[\%]$	$\frac{M_{\text{esc}}}{M_M}$	$\delta f_T[\%]$	$\delta_{\text{enrich}}$	$Q_{\text{tar,solid}}$	$Q_{\text{imp}}$	$\frac{M_m}{M_M}$
<i>Lrf12</i> <sub>Solid</sub>	-0.30	20	2.3	2.68	0.09	0.65	1.2	2.71	-11	0.00	0.55	5.39	0.18
<i>Lrf12</i> <sub>Molten</sub>	-0.30	20	2.3	2.68	0.06	0.44	0.6	2.69	-8	-0.02	0.30	6.09	0.12
<i>Lrf1</i> <sub>Molten*</sub>	-0.30	23	2.3	2.62	0.10	0.81	0.6	3.50	2	0.02	1.22	-9.29	0.18
<i>Lrf2</i> <sub>Molten*</sub>	-0.40	10	2.3	2.84	0.04	0.34	0.0	0.93	-11	-0.03	0.32	4.97	0.09
<i>Lrf3</i> <sub>Molten*</sub>	-0.50	10	2.3	2.79	0.02	0.17	0.0	1.03	-10	-0.03	0.30	5.41	0.04
<i>Lrf4</i> <sub>Molten*</sub>	-0.30	10	2.5	2.31	0.02	0.14	0.0	0.62	-6	-0.01	0.00	8.61	0.03
<i>Lrf5</i> <sub>Molten*</sub>	-0.30	10	3.0	2.31	0.02	0.14	0.0	0.62	-11	-0.02	0.30	4.89	0.03
<i>Lrf6</i> <sub>Molten</sub>	0.00	23	3.0	1.43	0.01	0.11	0.0	2.12	-4	0.00	-1.00	18.73	0.01
<i>Lrf7</i> <sub>Molten</sub>	0.00	10	3.0	1.50	0.00	0.01	0.0	0.13	0	0.05	0.84	-1.78	0.00
<i>Lrf8</i> <sub>Solid</sub>	0.00	20	3.0	1.47	0.00	0.04	0.0	1.27	-16	0.00	0.56	4.15	0.00
<i>Lrf8</i> <sub>Molten</sub>	0.00	20	3.0	1.47	0.00	0.03	0.9	1.15	-8	-0.01	0.13	6.47	0.00
<i>Lrf9</i> <sub>Molten</sub>	-0.30	10	3.0	1.31	0.00	0.02	0.0	0.39	-67	-0.22	0.56	1.51	0.00
<i>Lrf10</i> <sub>Solid</sub>	-0.30	20	3.0	1.14	0.00	0.03	0.0	1.89	-15	0.00	0.60	4.25	0.00
<i>Lrf10</i> <sub>Molten</sub>	-0.30	20	3.0	1.14	0.00	0.03	0.0	1.91	-7	-0.01	0.07	8.23	0.00
<i>Lrf11</i> <sub>Solid</sub>	-0.30	20	2.5	2.12	0.02	0.14	0.2	2.26	-8	0.00	0.30	7.06	0.04
<i>Lrf11</i> <sub>Molten</sub>	-0.30	20	2.5	2.12	0.01	0.09	0.0	2.29	-9	-0.02	0.27	5.86	0.03
<i>Lrf13</i> <sub>Solid</sub>	-0.50	20	2.3	2.56	0.05	0.40	2.0	3.08	-7	0.00	0.34	8.23	0.12
<i>Lrf13</i> <sub>Molten</sub>	-0.50	20	2.3	2.56	0.05	0.37	2.6	3.27	-9	-0.02	0.33	5.97	0.10
<i>Lrf14</i> <sub>Solid</sub>	-0.50	20	2.5	2.00	0.01	0.06	2.5	2.73	-17	0.00	0.71	3.92	0.01
<i>Lrf14</i> <sub>Molten</sub>	-0.50	20	2.5	1.99	0.01	0.04	3.1	2.89	-8	-0.02	0.30	6.15	0.01
<i>Lrf15</i> <sub>Solid</sub>	0.30	10	3.0	1.71	0.00	0.04	0.0	0.17	-41	0.00	0.83	2.19	0.01
Simulations run as in the fast-spinning case using the double-layered proto-Earth model													
Run	$b$	$v_{\text{imp}}$	$P_{\text{tar}}$	$\frac{L_{\text{sys}}}{L_{\text{EM}}}$	$\frac{L_D}{L_{\text{EM}}}$	$\frac{M_D}{M_M}$	$\delta_{\text{FE}}[\%]$	$\frac{M_{\text{esc}}}{M_M}$	$\delta f_T[\%]$	$\delta_{\text{enrich}}$	$Q_{\text{tar,solid}}$	$Q_{\text{imp}}$	$\frac{M_m}{M_M}$
<i>Lrdf1</i> <sub>Solid</sub>	-0.30	20	2.3	2.70	0.09	0.72	1.4	2.28	-9	0.0	0.82	6.27	0.20
<i>Lrdf2</i> <sub>Solid</sub>	-0.30	30	2.3	2.70	0.08	0.58	1.2	2.45	-8	0.0	0.79	7.38	0.16
<i>Lrdf3</i> <sub>Solid</sub>	-0.30	10	2.3	2.37	0.08	0.62	1.9	8.09	-4	0.0	0.66	12.58	0.16
<i>Lrdf4</i> <sub>Solid</sub>	0.00	10	2.3	2.92	0.11	0.83	0.3	0.81	-18	0.0	0.90	3.81	0.28
<i>Lrdf5</i> <sub>Solid</sub>	0.00	20	2.3	3.09	0.07	0.49	0.3	0.60	-21	0.0	0.90	3.40	0.17
<i>Lrdf6</i> <sub>Solid</sub>	-0.15	20	2.3	2.97	0.07	0.53	2.4	2.45	-11	0.0	0.84	5.37	0.19
<i>Lrdf1</i> <sub>Solid</sub> <sup>x3</sup>	-0.30	20	2.3	2.84	0.11	0.80	2.9	2.18	-10	0.0	0.82	6.13	0.23

**Notes.** All the different cases consist of  $N = 3.1 \times 10^5$  SPH particles. *Lrf*# signifies simulations run with the PES and PEM models, *Lrdf*# represents simulations run with the two-layered model, and *Lrdf1*<sub>Solid</sub><sup>x3</sup> is a *df*# simulation in which we have tripled the vaporization energy. The \* at the end of some run names signifies simulations that were run with constant AV parameters ( $\alpha = 1, \beta = 2$ ). Here,  $b$  is the impact parameter,  $v_{\text{imp}}$  is the impact speed in kilometres per second,  $P_{\text{tar}}$  is the spin period of the target planet in hours,  $L_{\text{sys}}$  is the angular momentum of the bound system,  $L_D$  is the angular momentum of the disk,  $M_D$  is the disk mass,  $\delta_{\text{FE}}$  is the iron content of the disk,  $M_{\text{esc}}$  escaping mass, and  $M_m$  is the estimated mass of the resulting moon. The parameters are scaled by angular momentum of the Earth–Moon system ( $L_{\text{EM}}$ ) and by the mass of the Moon ( $M_M$ ). The compositional parameters ( $\delta f_T, \delta_{\text{enrich}}, Q_{\text{imp}}, Q_{\text{tar,solid}}$ ) are all defined in Sect. 3.

smaller disk mass and angular momentum. This ocean slightly increases the mixing of the resulting Moon which decreases  $|\delta f_T|$  and is what we first predicted would occur from the increased pressure gradients due to asymmetric heating of the molten surface. However, the effect is mild; it would be interesting to investigate whether or not the effect becomes more prominent with a deeper molten ocean. Additionally, for silicate liquids the Gruneisen parameter has been observed to increase under pressure (Mosenfelder et al. 2009). In this paper we approximate this by using a higher ambient Gruneisen parameter for the molten material, but it might be that we still underestimate the effective heating and pressure from the molten surface. In the low-resolution cases, the effect of the molten ocean is not significant and is likely due to not resolving the molten ocean properly. However, dynamically, the low- and high-resolution cases are relatively close, leading to similar post-impact properties, with

higher resolution and slightly larger Moon masses. Comparing the multi-layered proto-Earth simulations to the simple-layered proto-Earth simulations we can see that the same trends persist. However, due to the larger size of the simple-layered proto-Earth the same impact angular momentum corresponds to a smaller impact velocity, which can drastically reduce the amount of material that ends up in the disk (comparing the *Hrc1*<sub>Solid</sub> to *Hdrcl1*<sub>Solid</sub> for example). Slightly increasing the impact velocity results in a much more massive Moon and with system properties that are more in line with the results of the multi-layered model. The multi-layered model does seem to in general confer more angular momentum to the disk for a given final angular momentum of the bound system. A curious result can be seen for the high impact-angular-momentum case (*Hdrc3* with  $L_{\text{imp}}/L_{\text{EM}} = 1.43$ ), in which the final Moon mass between the *Hdrc3*<sub>Solid</sub> and *Hdrc3*<sub>Molten</sub> simulations differs by a significant

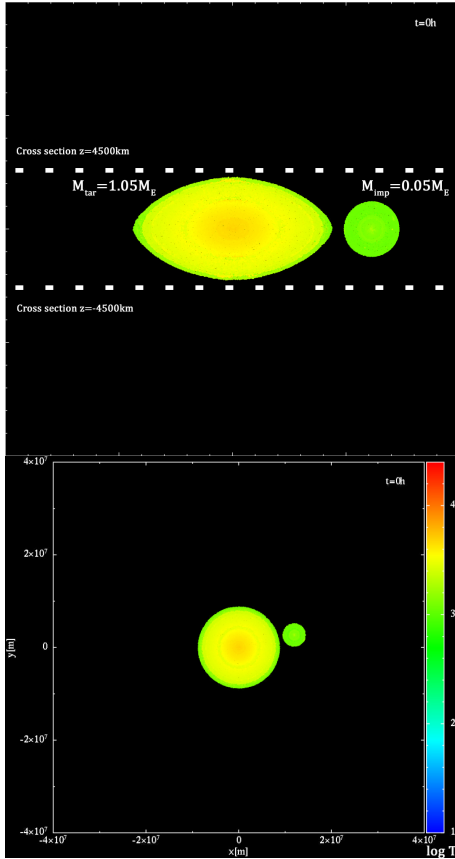


**Fig. 12.** Initial setup of the  $Lrf12_{\text{Molten}}$  simulation. The impact parameter, impact velocity, and spin of the target planet is in this case set to  $b = -0.3$ ,  $v_{\text{imp}} = 20 \text{ km s}^{-1}$  and  $P_{\text{tar}} = 2.3 \text{ h}$  respectively. The color rendering represents the temperature. *Upper figure:* equatorial view of the initial setup. The cross section that can be seen represents the region in which particles are rendered, which is done to improve the clarity of the following figures. *Lower figure:* top-down view of the initial setup and is the viewpoint in the upcoming figures.

factor. This is mainly due to the escape of a large satellite from the bound system in the  $Hdrc3_{\text{Molten}}$  simulation (similar in size to the one seen in Fig. 6e). Interestingly, in  $Hdrc3_{\text{Molten}}$  the final system properties suggest a quite dynamically successful Moon-forming impact with  $L_{\text{sys}} = 1.12$  and  $M_m = 1.19$ . Recently, Hosono et al. (2019) presented results from numerical simulations done with a terrestrial magma ocean, where they show that a significant portion of the lunar-forming material is derived from the magma ocean. This is different from the results that we present in the present paper, and there are a few key differences between our simulations and those of these latter authors that can play a significant role. The first difference is the use of an alternative formulation of SPH, called DISPH (Saitoh & Makino 2013), which has been shown to improve gradient accuracy at contact discontinuity and allow for more efficient mixing of materials. This is likely the major factor that affects the results, as in Hosono et al. (2019) a target-dominated disk was not seen when using regular SPH, which is consistent with our results. The second difference is the use of a deeper magma ocean than the one presented here, ranging in depth from about 500 to 2000 km. Another potential factor is the difference in equations of state, where Hosono et al. (2019) use a double EOS model for their impact. The molten silicate is accurately modeled with a hard-sphere model (Jing & Karato 2011), which correctly captures

the increase in the Gruneisen parameter during compression. However, the rest of the planetary material is modeled with the Tillotson EOS (Tillotson 1962), which has been shown to be inappropriate for high-energy impacts where there is significant vaporization. This is mainly due to the lack of a proper vapor transition which leads to erroneous decompression velocities as shown in Stewart et al. (2019). The result of our canonical simulations follows closely the trend from Canup (2004), with the most successful Moon-forming impacts occurring in the range  $b = 0.7 \leftrightarrow 0.76$ . The biggest difference in our results compared to those of Canup (2004) is that we get larger disk masses (about a 20% increase). The biggest effect is likely due to the artificial viscosity switch implementation which has been predicted to increase disk mass to about 10%. We can see that there is a certain linear relationship between the impact parameter and the resulting Moon mass. At a low impact parameter, we require a large impact velocity to create the desired angular momentum. This significantly disrupts the target planet and a lot of material escapes the system; these simulations also result in a more iron-rich disk. The introduction of an icy impactor resulted in quite different results. First, we got a large increase in resulting Moon masses in the range  $b = 0.67 \leftrightarrow 0.8$ . However, this drops quite rapidly when going below an impact parameter of 0.6. This is because there is a quite drastic increase in the amount of mass that escapes the system (see Fig. 11b). Another effect of the icy impactor is that the disk becomes even more dominated with impactor material (see Fig. 11c). This makes it highly unlikely that an icy impactor would be able to create the right conditions for the Earth–Moon system in these sorts of collisions. This is the main reason why we opted not to run higher resolution simulations for this case.

From our simulations of the fast-spinning case, we can see that we were not able to recreate the results of Čuk & Stewart (2012), or those of Nakajima & Stevenson (2014). Both of these authors apply the M-ANEOS equation of state (Thompson & Lauson 1972; Melosh 2007) and similar impact parameters. Taking a closer look at their data, we can see that even though we have similar angular momentum in the whole collision, only a very small fraction resides in the disk. We can see that our disk mass is almost two to three times lower. This large discrepancy is quite curious and implies that there is something that has a large effect on this kind of collision. It could be that the collision is very sensitive to the initial conditions and that because we use PREM material parameters for the inner regions, we get an impactor and planet that is less dense. A more compact impactor would first of all penetrate deeper into the planet leading to larger pressure wave bulges being formed that in turn fling more material into orbit. Making the impactor more compact would also decrease the amount of material that is scattered by the target planet (see Fig. 17), because these scattered particles have very low angular momentum (in  $z$ ). We also tested a simpler double-layered model for proto-Earth and increased the vaporization energy for the materials. None of these tests changed the results significantly (Fig. 18). The simulations of the fast-spinning case do in general show less disk–planet deviation  $\delta f_T > -20\%$  (Fig. 18c), which constricts realistic combinations of target and impactor  $Q$  values and leads to only a handful of impacts that have acceptable  $Q$  values (Fig. 18d).

We now consider the two density profiles of the different cases in Figs. 8 and 15. As we can see from these figures, the two kinds of impacts result in very different disk structures. For the canonical case we are left with a disk-like structure. In the fast-spinning case on the other hand, there is not really a disc structure, and instead we end up with a more isotropic

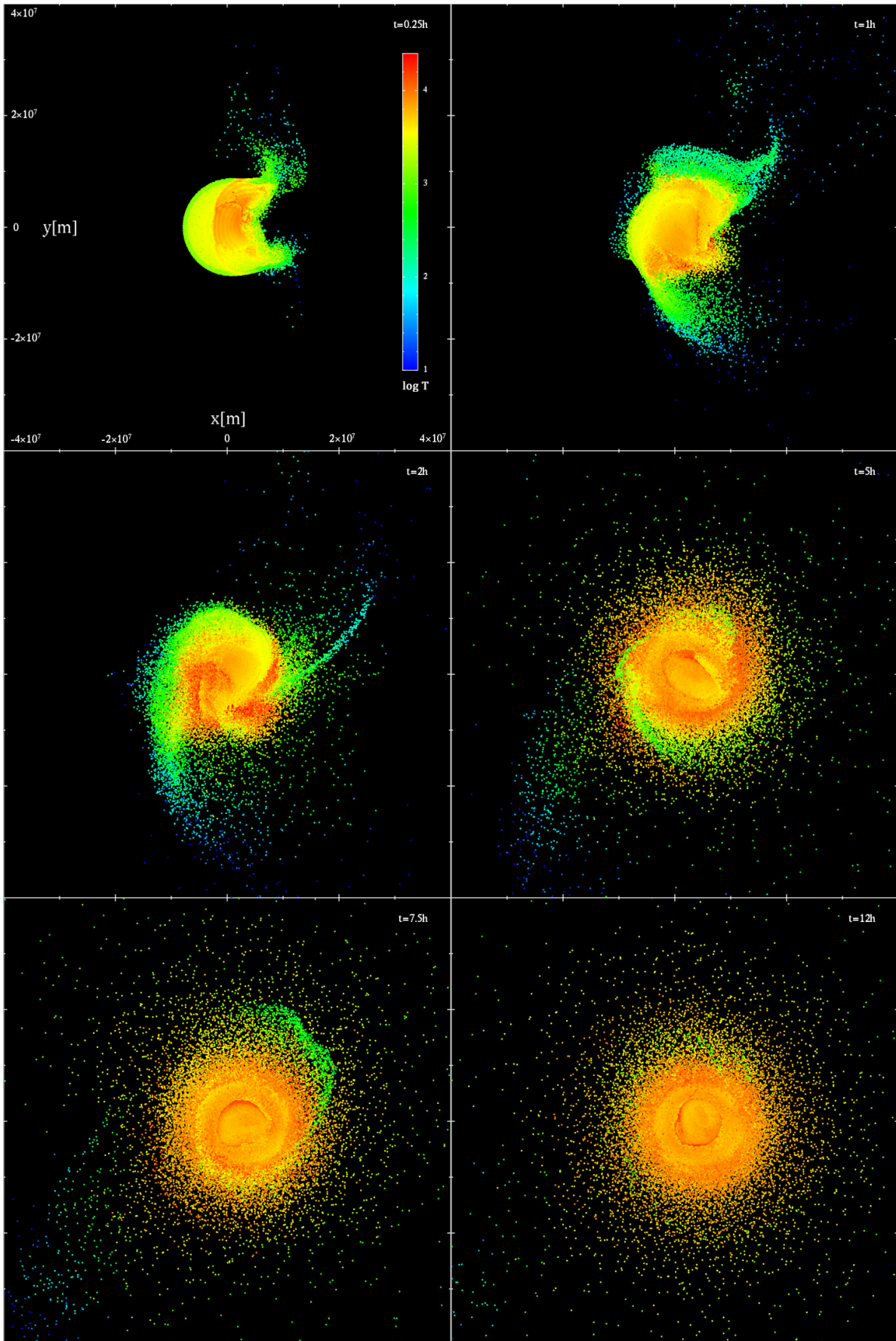


**Fig. 13.** Top-down view of the evolution of the collision of the  $Lrf12_{\text{Molten}}$  simulation. The temperature range and spatial range can be seen in the *top left panel*. The times at which the images were taken, starting from the upper left, are  $t = 0.25, 1, 2, 5, 7.5, 12$  h.

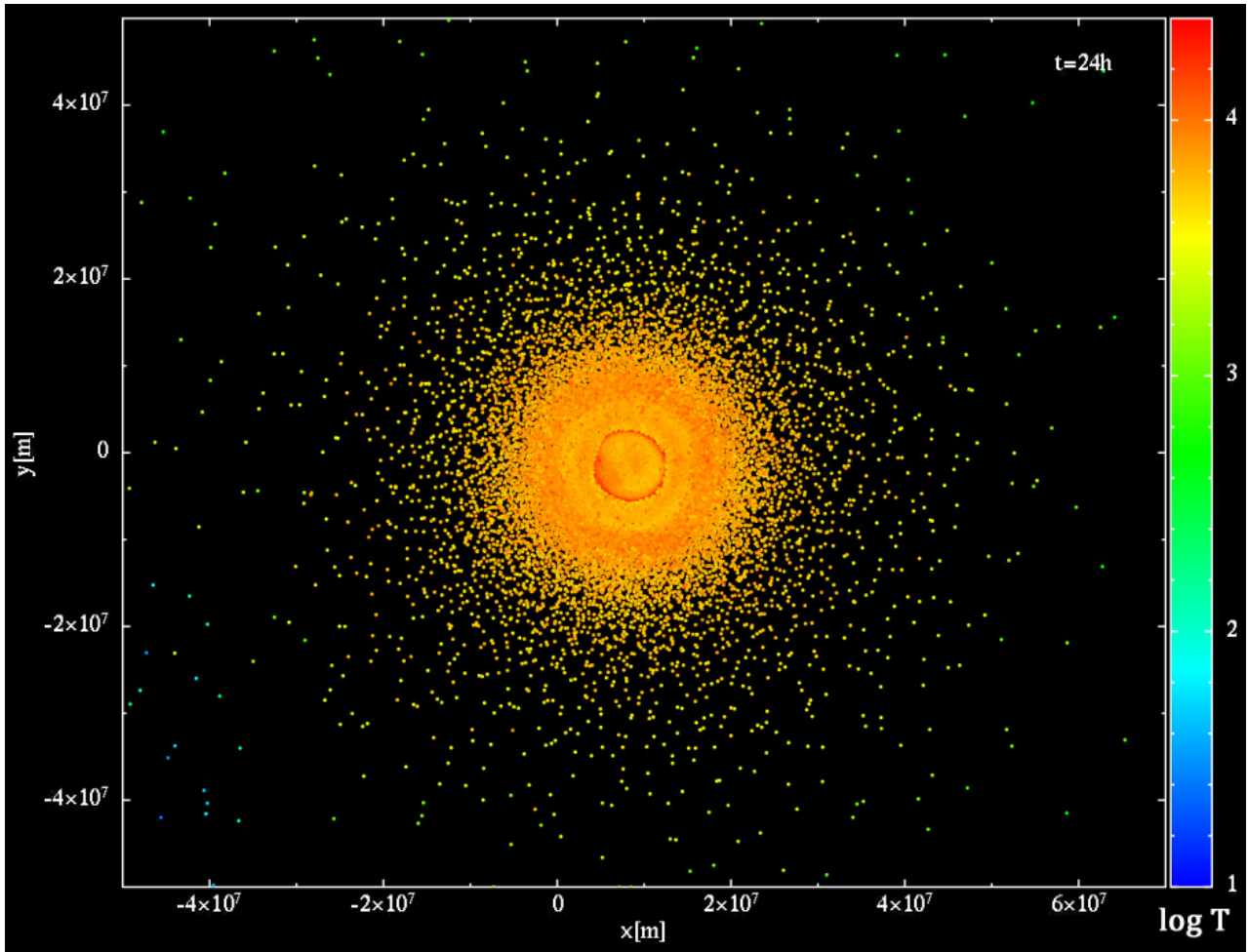


Fig. 14. State of the system after 24 h of simulation time.

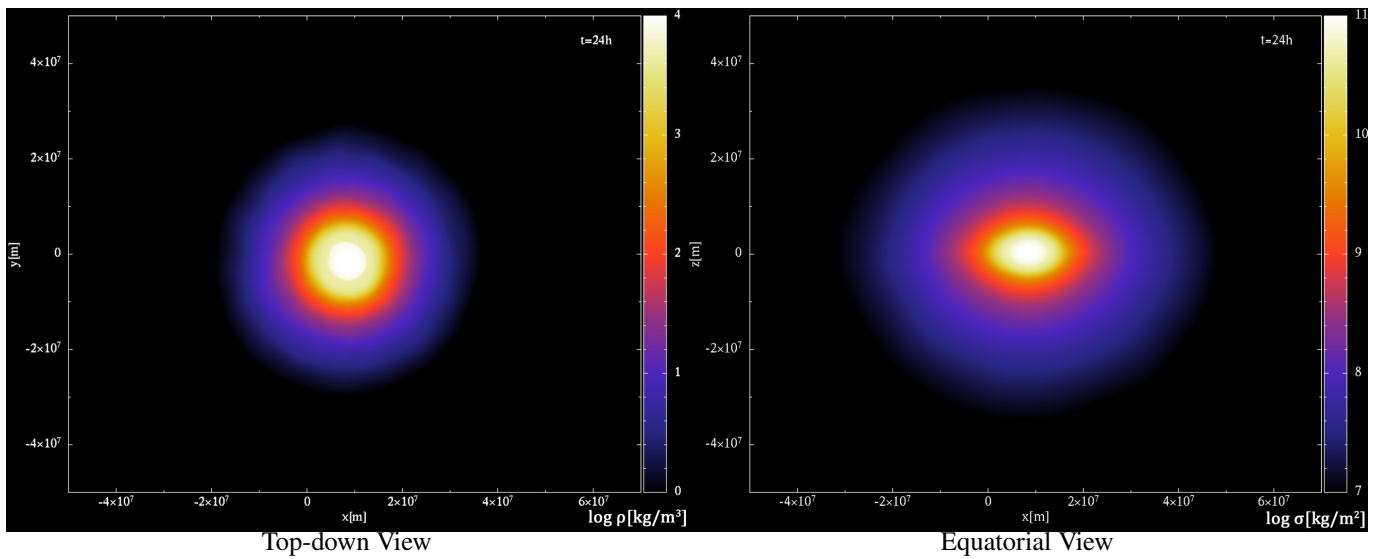
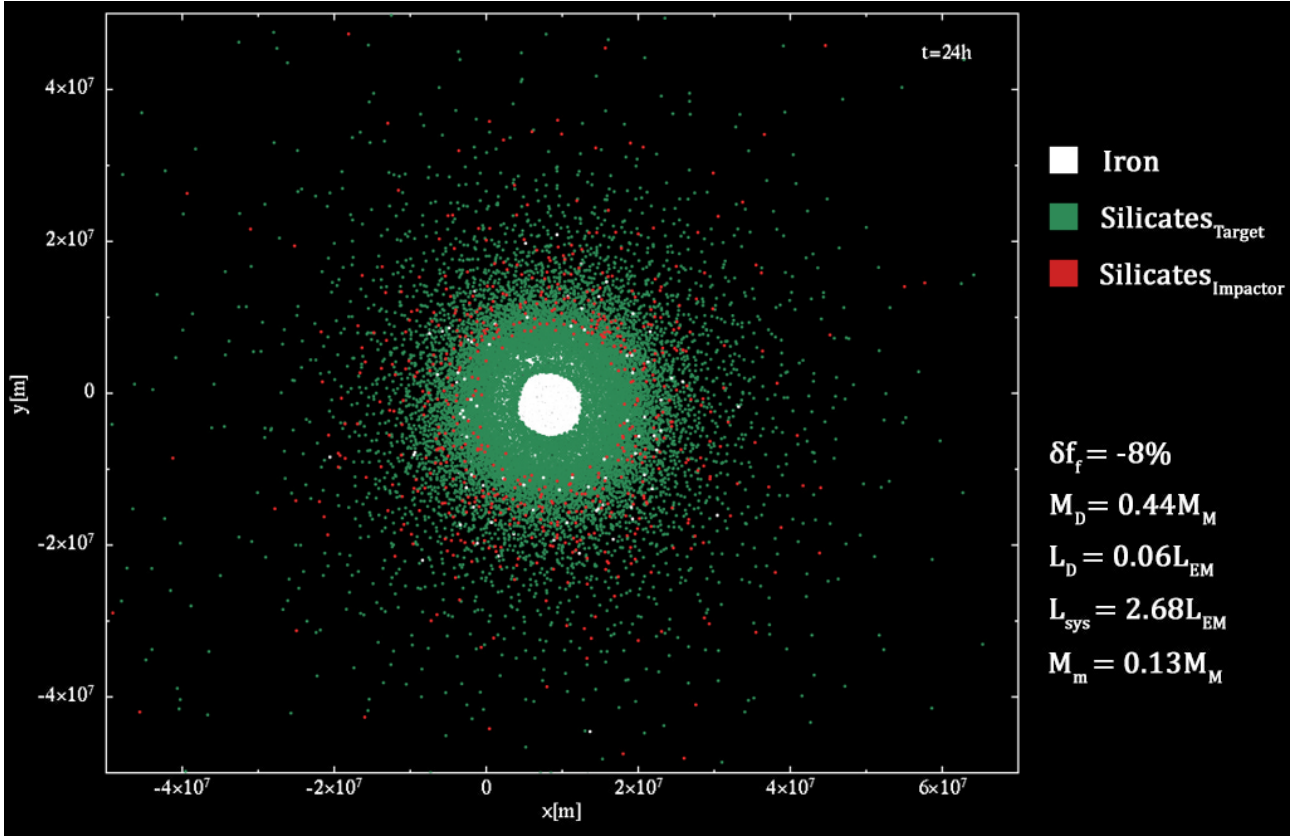
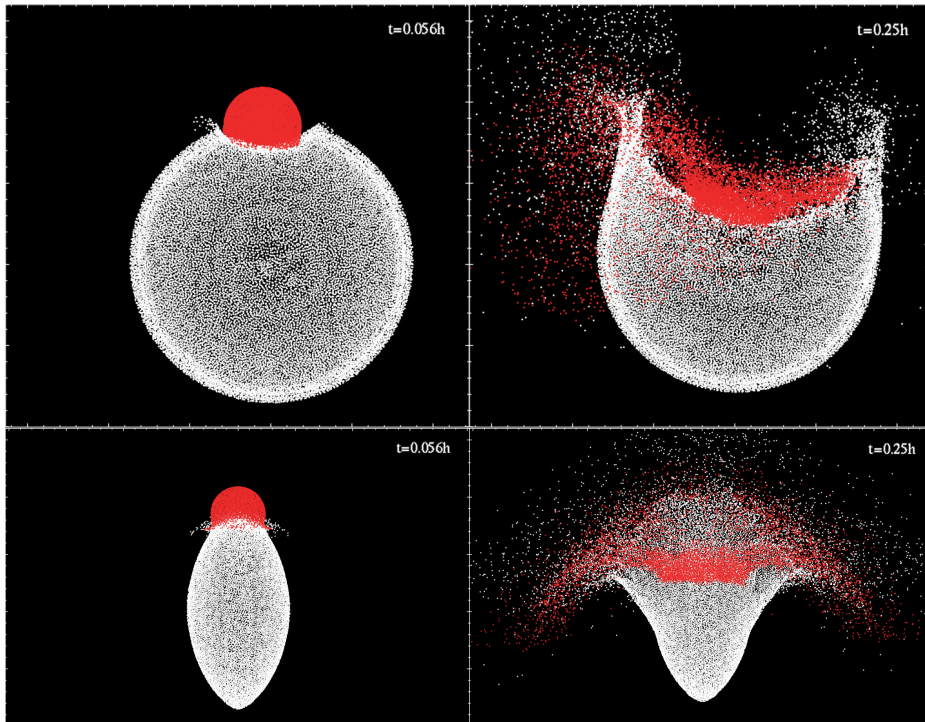


Fig. 15. Density rendering of the system after 24 h of simulation time. No real disk-like structure can be seen, the material appears evenly stratified around a fast-spinning inner core. The color rendering on the *right picture* represents the column density.



**Fig. 16.** Compositional analysis after 24 h of simulation time. Colors denote the different materials and origins. We can see that the target and impactor material are very evenly and isotropically distributed in the disk. Assuming no mass loss from the subsequent disk evolution we get an estimated Moon mass of  $M_m = 0.13M_M$ .



**Fig. 17.** Two snapshots from different viewing angles of the impactor penetrating into the target planet. *Upper figure:* top-down view and *bottom figure:* equatorial view. The impactor is fully rendered in red and only the surface particles of the target planet are rendered in white. *Top panels:* impactor making a large crater and reaching the core of the planet. *Bottom figures:* show that there are quite a lot of particles that scatter out from the plane of collision.

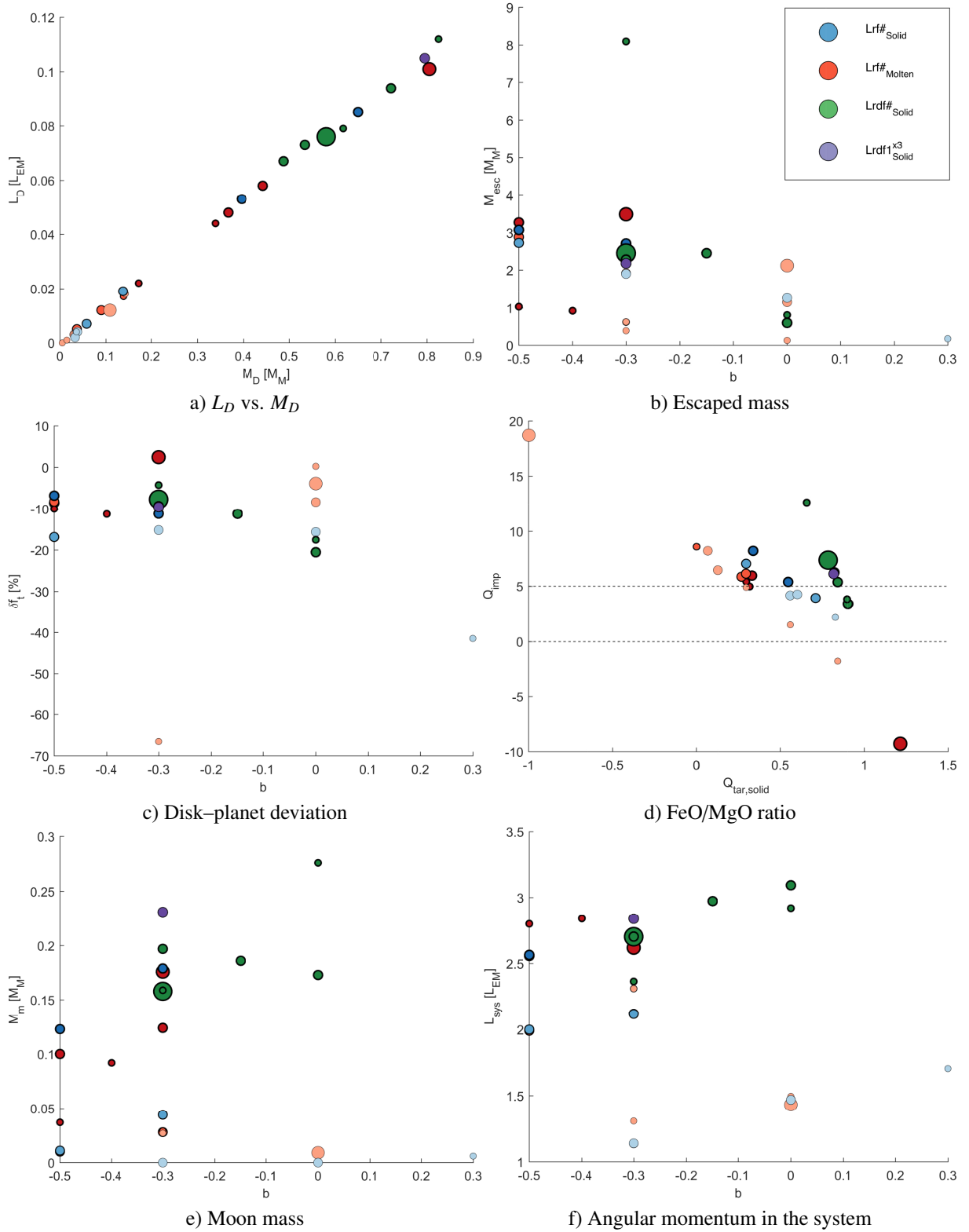


**Fig. 18.** Results from all the simulations in Table 2. The size of the symbols represents the impact velocity. The thickness of the surrounding black line represents the different initial spin periods, with the thickest being the 2.3 h case. The colors represent different proto-Earth models: the blue, red, green, and purple represent the PES, PEM, two-layered model, and the two-layered model with three times the vaporization energy respectively. The gradient in the color represents the estimated mass of the Moon relative to the distribution. The dashed lines in *panel d* represent the limits of the allowed compositional value of the impactor. The dashed line in *panel f* represents the angular momentum of the 2.3 h spinning planet. *Panel a*: linear relationship between the mass and angular momentum of the disk. *Panel c*: reveals that, in general, there is a small disk-planet deviation. *Panel d*: shows that most of the simulations result in unrealistic  $Q$  values which are outside the limits ( $0 < Q_{imp} < 5$ ). *Panels e and f*: show that we cannot create a Moon-like satellite in this case.

distribution. There does not seem to be any real distinction between the disk and the planet in this case. This raises the question of whether or not the method proposed by [Ida et al. \(1997\)](#) for estimating the disk mass and angular momentum is valid for this specific case. Because the disk is coupled to the vaporized atmosphere of the planet, the angular momentum considerations made by these latter authors should not be valid if the disk actively interacts with the atmosphere. This isotropic distribution of the final state can also be seen in the simulations of [Čuk & Stewart \(2012\)](#); [Lock & Stewart \(2017\)](#), where the authors further discuss the different aspects of this kind of final state. Additionally, the subsequent evolution of such a system has been studied in the work of [Lock et al. \(2018\)](#), where satellites with many of the main features of our Moon were reproduced.

The fitted lines to the  $L_d/M_d$  relationship that we see in Figs. 11a and 18a reveal how efficient the angular momentum transfer is in the collision. We can see that this parameter is the highest for the *Lrc#* model ( $M_m \approx 0.74M_D$ ) and the *Hdrc#* model ( $M_m \approx 0.73M_D$ ), followed by the *Lic#* model ( $M_m \approx 0.56M_D$ ), and is the lowest in the fast-spinning case ( $M_m \approx 0.3M_D$ ).

## 6. Conclusions

Our compositional analysis of the lunar-forming impact reveals that the classical models of a chemically uniform mantle are inconsistent with the current observed FeO/MgO difference between the Earth and the Moon. Either an additional source of enrichment is required or a Theia with near-identical Earth-like isotopic composition. An enstatite composition for Theia is still possible, but would require substantial mantle oxidation post-impact.

From our high-resolution canonical simulations we can conclude that a magma ocean of 300–500 km in depth slightly increases the mixing and results in a less massive Moon. The canonical simulations fit well with the dynamical aspects of the Earth–Moon system, with an impact parameter of around  $b=0.73$  and angular momentum of around  $L_{\text{imp}}=1.25L_{\text{EM}}$ . These simulations resulted in a high  $\delta f_T$  value, which means that we require a near Earth-like isotopic composition for Theia. These results agree well with the results from [Canup \(2004\)](#). The main trends are seen regardless of whether a multi-layered proto-Earth is used instead of a simple-layered proto-Earth. Although the simple-layered proto-Earth did in general produce smaller moon masses at a given impact angular momentum, we predict that this is mainly due to the increase in the radius of the simple-layered proto-Earth model, as the results were relatively sensitive to slight increases in the impact velocity. Using an icy Theia in the canonical model led to a higher  $\delta f_T$  value and a more massive Moon compared to using a rocky Theia. The high  $\delta f_T$  value makes this case very unlikely, as CI-chondrite requires a very low  $\delta f_T$  value to be compatible with observations. In regard to the fast-spinning case, our simulations were not able to produce a sufficiently massive Moon.

## References

- Abe, Y. 1997, *Phys. Earth Planet. Inter.*, 100, 27  
 Agertz, O., Moore, B., Stadel, J., et al. 2007, *MNRAS*, 380, 963  
 Asphaug, E., Collins, G., & Jutzi, M. 2015, *Global Scale Impacts*, eds. P. Michel, F. E. DeMeo, & W. F. Bottke (Tucson, AZ: University of Arizona Press), 661  
 Benz, W., Cameron, A. G. W., & Melosh, H. J. 1989, *Icarus*, 81, 113

- Bobrick, A., Davies, M. B., & Church, R. P. 2017, *MNRAS*, 467, 3556  
 Cameron, A. G. W., & Ward, W. R. 1976, *Lunar and Planetary Science Conference*, 7  
 Canup, R. M. 2004, *Icarus*, 168, 433  
 Canup, R. M. 2008a, *Icarus*, 196, 518  
 Canup, R. M. 2008b, *Lunar and Planetary Science Conference*, 2429  
 Canup, R. M. 2012, *Science*, 338, 1052  
 Canup, R. M., & Asphaug, E. 2001, *Nature*, 412, 708  
 Costa, G. C. C., Jacobson, N. S., & Fegley, Jr. B. 2017, *Icarus*, 289, 42  
 Čuk, M., & Stewart, S. T. 2012, *Science*, 338, 1047  
 Dauphas, N. 2017, *Nature*, 541, 521  
 Dehnen, W., & Aly, H. 2012, *MNRAS*, 425, 1068  
 Gingold, R. A., & Monaghan, J. J. 1977, *MNRAS*, 181, 375  
 Goldreich, P., Lithwick, Y., & Sari, R. 2004, *ApJ*, 614, 497  
 Hartmann, W. K., & Davis, D. R. 1975, *Icarus*, 24, 504  
 Herwartz, D., Pack, A., Friedrichs, B., & Bischoff, A. 2014, *Science*, 344, 1146  
 Hosono, N., Karato, S.-i., Makino, J., & Saitoh, T. R. 2019, *Nat. Geosci.*, 12, 418  
 Ida, S., & Makino, J. 1993, *Icarus*, 106, 210  
 Ida, S., Canup, R. M., & Stewart, G. R. 1997, *Nature*, 389, 353  
 Javoy, M. 1995, *Geophys. Res. Lett.*, 22, 2219  
 Jing, Z., & Karato, S.-i. 2011, *Geochim. Cosmochim. Acta*, 75, 6780  
 Jones, J. H., & Palme, H. 2000, *Origin of the Earth and Moon*, eds. R. M. Canup, & K. Righter (Tucson, AZ: University of Arizona Press), 197  
 Kaib, N. A., & Cowan, N. B. 2015, *Icarus*, 252, 161  
 Karato, S.-i. 2014, *Proc. Jpn. Acad. Ser. B*, 90, 97  
 Kokubo, E., Ida, S., & Makino, J. 2000, *Icarus*, 148, 419  
 Lock, S. J., & Stewart, S. T. 2017, *J. Geophys. Res. Planets*, 122, 950  
 Lock, S. J., Stewart, S. T., Petaev, M. I., et al. 2018, *J. Geophys. Res. Planets*, 123, 910  
 Lucy, L. B. 1977, *AJ*, 82, 1013  
 Mastrobuono-Battisti, A., Perets, H. B., & Raymond, S. N. 2015, *Nature*, 520, 212  
 McKinnon, W. B. 2008, *Bull. Am. Astron. Soc.*, 40, 464  
 Meier, M. M. M., Reufer, A., & Wieler, R. 2014, *Icarus*, 242, 316  
 Melosh, H. J. 2007, *Meteorit. Planet. Sci.*, 42, 2079  
 Melosh, H. J. 2009, *Meteorit. Planet. Sci. Suppl.*, 72, 5104  
 Mibe, K., Fujii, T., Yasuda, A., & Ono, S. 2006, *Geochim. Cosmochim. Acta*, 70, 757  
 Morris, J. P., & Monaghan, J. J. 1997, *J. Comput. Phys.*, 136, 41  
 Mosenfelder, J. L., Asimow, P. D., Frost, D. J., Rubie, D. C., & Ahrens, T. J. 2009, *J. Geophys. Res. Solid Earth*, 114, B01203  
 Nakajima, M., & Stevenson, D. J. 2014, *Icarus*, 233, 259  
 Pahlevan, K., & Stevenson, D. J. 2007, *Earth Planet. Sci. Lett.*, 262, 438  
 Pahlevan, K., Stevenson, D. J., & Eiler, J. M. 2011, *Earth Planet. Sci. Lett.*, 301, 433  
 Park, R. S., Konopliv, A. S., Bills, B. G., et al. 2016, *Nature*, 537, 515  
 Price, D. J. 2007, *PASA*, 24, 159  
 Rasio, F. A., & Lombardi, Jr. J. C. 1999, *J. Comput. Appl. Math.*, 109, 213  
 Reinhardt, C., & Stadel, J. 2017, *MNRAS*, 467, 4252  
 Reufer, A., Meier, M. M. M., Benz, W., & Wieler, R. 2012, *Icarus*, 221, 296  
 Saff, E. B., & Kuijlaars, A. B. J. 1997, *Math. Intell.*, 19, 5  
 Saitoh, T. R., & Makino, J. 2013, *ApJ*, 768, 44  
 Sasaki, S., & Nakazawa, K. 1986, *J. Geophys. Res.*, 91, 9231  
 Stewart, S. T., Davies, E. J., Duncan, M. S., et al. 2019, ArXiv e-prints [arXiv:1910.04687]  
 Stixrude, L., & Lithgow-Bertelloni, C. 2005, *Geophys. J. Int.*, 162, 610  
 Thomas, P. C., Parker, J. W., McFadden, L. A., et al. 2005, *Nature*, 437, 224  
 Thomas, C. W., Liu, Q., Agee, C. B., Asimow, P. D., & Lange, R. A. 2012, *J. Geophys. Res. Solid Earth*, 117, B10206  
 Thompson, S. L., & Lauson, H. S. 1972, Improvements in the Chart D Radiation-Hydrodynamic Code. III: Revised Analytic Equations of State, Tech. rep.  
 Tillotson, J. H. 1962, General Atomic Report GA-3216  
 Touma, J., & Wisdom, J. 1998, *AJ*, 115, 1653  
 Wade, J., & Wood, B. J. 2005, *Earth Planet. Sci. Lett.*, 236, 78  
 Walsh, K. J., Morbidelli, A., Raymond, S. N., O'Brien, D. P., & Mandell, A. M. 2011, *Nature*, 475, 206  
 Warren, P. H. 2005, *Meteorit. Planet. Sci.*, 40, 477  
 Warren, P. H., & Dauphas, N. 2014, *Lunar Planet. Sci. Conf.*, 45, 2298  
 Weppner, S. P., McKelvey, J. P., Thielen, K. D., & Zielinski, A. K. 2015, *MNRAS*, 452, 1375  
 Wetzstein, M., Nelson, A. F., Naab, T., & Burkert, A. 2009, *ApJS*, 184, 298  
 Wiechert, U., Halliday, A. N., Lee, D.-C., et al. 2001, *Science*, 294, 345  
 Zhang, J., Dauphas, N., Davis, A. M., Leya, I., & Fedkin, A. 2012, *Nat. Geosci.*, 5, 251

## Appendix A: Planetary models

Below are the models used in the simulations.

### A.1. Proto-Earth models

Ic = Inner core Oc = Outer core Lm = Lower mantle Um = Upper mantle Mo = Molten ocean

**Table A.1.** PES Multi-layered Model 1  $M = 1.05M_E$   $P_C = 378$  GPa  $T_C = 5400$  K.

Layer	$\rho_0$	$B_0$	$B'_0$	$A$	$Z$	$t_{\min}$	$\delta_t$	$\gamma_0$	$q_0$	$T_l$	$r_l$ [km]
Ic	7744	166e9	5.1	55	26	1.8	2	1.78	0.69	5246	1221.5
Oc	6920	115e9	5.4	55	26	1.8	2	1.93	0.58	4070	3420
Lm	4121	231e9	4.0	36	18	1	1.4	1.5	1.53	1783	5641
Um	3300	130e9	4.2	36	18	2.2	13	1.2	2.25	1488	6610

**Table A.2.** PEM Multi-layered Model 1  $M = 1.05M_E$   $P_C = 385$  GPa  $T_C = 5400$  K.

Layer	$\rho_0$	$B_0$	$B'_0$	$A$	$Z$	$t_{\min}$	$\delta_t$	$\gamma_0$	$q_0$	$T_l$	$r_l$ [km]
Ic	7744	166	5.1	55	26	1.8	2	1.78	0.69	5248	1221.5
Oc	6920	115	5.4	55	26	1.8	2	1.93	0.58	4085	3420
Lm	4121	231	4.0	36	18	1	1.4	1.5	1.53	3165	5641
Um	3300	130	4.2	36	18	2.2	13	1.2	2.25	2865	6200
Mo	2800	23	6.2	36	18	2.2	0	2.2	-0.17	2079	6671

**Table A.3.** PES Two-layered Model 1  $M = 1.05M_E$   $P_C = 377$  GPa  $T_C = 5200$  K.

Layer	$\rho_0$	$B_0$	$B'_0$	$A$	$Z$	$t_{\min}$	$\delta_t$	$\gamma_0$	$q_0$	$T_l$	$r_l$ [km]
Core	7744	166	5.1	55	26	1.8	2	1.78	0.69	3903	3380
Mantle	3300	130	4.2	36	18	2.2	13	1.2	2.25	1296	6850

**Table A.4.** PES Multi-layered Model 2  $M = 0.95M_E$   $P_C = 354$  GPa  $T_C = 5400$  K.

Layer	$\rho_0$	$B_0$	$B'_0$	$A$	$Z$	$t_{\min}$	$\delta_t$	$\gamma_0$	$q_0$	$T_l$	$r_l$ [km]
Ic	7744	166	5.1	55	26	1.8	2	1.78	0.69	5241	1221.5
Oc	6920	115	5.4	55	26	1.8	2	1.93	0.58	4013	3420
Lm	4121	231	4.0	36	18	1	1.4	1.5	1.53	1749	5641
Um	3300	130	4.2	36	18	2.2	13	1.2	2.25	1526	6210

**Table A.5.** PEM Multi-layered Model 2  $M = 0.95M_E$   $P_C = 361$  GPa  $T_C = 5400$  K.

Layer	$\rho_0$	$B_0$	$B'_0$	$A$	$Z$	$t_{\min}$	$\delta_t$	$\gamma_0$	$q_0$	$T_l$	$r_l$ [km]
Ic	7744	166	5.1	55	26	1.8	2	1.78	0.69	5243	1221.5
Oc	6920	115	5.4	55	26	1.8	2	1.93	0.58	4030	3420
Lm	4121	231	4.0	36	18	1	1.4	1.5	1.53	3062	5641
Um	3300	130	4.2	36	18	2.2	13	1.2	2.25	2890	5950
Mo	2800	23	6.2	36	18	2.2	0	2.2	-0.17	2137	6310

**Table A.6.** PES Simple-layered Model 2  $M = 0.95M_E$   $P_C = 354$  GPa  $T_C = 5400$  K.

Layer	$\rho_0$	$B_0$	$B'_0$	$A$	$Z$	$t_{\min}$	$\delta_t$	$\gamma_0$	$q_0$	$T_l$	$r_l$ [km]
Ic	7744	166	5.1	55	26	1.8	2	1.78	0.69	3999	3380
Um	3300	130	4.2	36	18	2.2	13	1.2	2.25	1326	6430

**Table A.7.** PEM Simple-layered Model 2  $M = 0.95M_E$   $P_C = 362$  GPa  $T_C = 5400$  K.

Layer	$\rho_0$	$B_0$	$B'_0$	$A$	$Z$	$t_{\min}$	$\delta_t$	$\gamma_0$	$q_0$	$T_l$	$r_l$ [km]
Ic	7744	166	5.1	55	26	1.8	2	1.78	0.69	4018	3380
Um	3300	130	4.2	36	18	2.2	13	1.2	2.25	2931	6100
Mo	2800	23	6.2	36	18	2.2	0	2.2	-0.17	2049	6540

### A.2. Theia

**Table A.8.** Rocky Model 1  $M = 0.05M_E$   $P_C = 33.7$  GPa  $T_C = 1300$  K.

Layer	$\rho_0$	$B_0$	$B'_0$	$A$	$Z$	$t_{\min}$	$\delta_t$	$\gamma_0$	$q_0$	$T_l$	$r_l$ [km]
Core	7744	166	5.1	55	26	1.8	2	1.78	0.69	1151	1370
Mantle	3300	130	4.2	36	18	2.2	13	1.2	2.25	1054	3391

**Table A.9.** Rocky model 2  $M = 0.142M_E$   $P_C = 71.9$  GPa  $T_C = 1800$  K.

Layer	$\rho_0$	$B_0$	$B'_0$	$A$	$Z$	$t_{\min}$	$\delta_t$	$\gamma_0$	$q_0$	$T_l$	$r_l$ [km]
Core	7744	166	5.1	55	26	1.8	2	1.78	0.69	1495	1900
Mantle	3300	130	4.2	36	18	2.2	13	1.2	2.25	1275	4000

**Table A.10.** Icy model  $M = 0.142M_E$   $P_C = 18.6$  GPa  $T_C = 500$  K.

Layer	$\rho_0$	$B_0$	$B'_0$	$A$	$Z$	$t_{\min}$	$\delta_t$	$\gamma_0$	$q_0$	$T_l$	$r_l$ [km]
Core	2379	78.8	5.37	15	12	2.5	0	1.69	-0.23	421	3700
Mantle	1689	40.5	6.25	29	24	2.5	0	2.13	-0.33	364	4494

## Appendix B: Shell distribution method

The number of particles per shell is determined by the surrounding mass:

$$N = \frac{M_{i+1} - M_i}{m_0} = \frac{4\pi}{m} \int_{r_i}^{r_{i+1}} \rho r^2 dr. \quad (\text{B.1})$$

Here,  $r_i$  is not the position of the shells, but instead the mass boundaries that surround each shell. These boundaries go from  $r = 0$  to  $r = R$  in which each mass boundary position is given by:

$$r_{i+1} = r_i + l_i, \quad (\text{B.2})$$

where  $l_i$  determines the mass boundary distance. Each shell is placed halfway between each mass boundary:

$$s_{i+1} = s_i + l_i/2. \quad (\text{B.3})$$

To determine the distance  $l_i$  between each mass boundary we begin first by calculating the mean particle distance in the current layer (inspired by [Bobrick et al. 2017](#)):

$$\delta_l = \left( \frac{Cm_0}{\langle \rho \rangle_l} \right)^{1/3}. \quad (\text{B.4})$$

Here, the  $l$  subscript represents the current layer,  $C$  is a constant, and  $\langle \rho \rangle_l$  is the mean density of the layer. The number of shells in this layer is then given by:

$$n_s = \frac{r_l}{\delta_l}, \quad (\text{B.5})$$

which is rounded to an integer number and then used to recalculate  $\delta_l = r_l/n$ . This is acceptable for a one-layer planet or a layer with small density discontinuities. However, for planets with large density discontinuities we add one extra term to the equation:

$$\epsilon_l = K \delta_l \frac{\Delta \rho_l}{\max(\Delta \rho_l)}, \quad (\text{B.6})$$

where  $K$  is a constant that is adjusted to fit with the SPH density approximation for the largest density drop in the planet  $\max(\Delta \rho_l)$ . This was found to lead to good fits with any other density discontinuity found in the planet ( $\Delta \rho_l$ ). We can then use epsilon to once again recalculate  $\delta_l$ .

$$\delta_l = \frac{n \delta_l - \epsilon_l \sum_{k=1}^{n_s} \frac{1}{k}}{n_s}. \quad (\text{B.7})$$

The length  $l_i$  is finally then given by:

$$l_i = \delta_l \frac{\epsilon_l}{(n_s + 1) - i}. \quad (\text{B.8})$$

The “ $i$ ” subscript represents the current shell. The constant  $C$  given above can be adjusted to give more or less shells.

### Appendix C: Compositional analysis method

The compositional deviation from the Earth can be quantified using the  $\epsilon$  notation:

$$\epsilon_i = \frac{\Delta_E - \Delta_i}{\Delta_E} \cdot 10\,000, \quad (\text{C.1})$$

where  $\Delta$  represents the ratio between two compositions and the subscript  $E$  signifies Earth values. The epsilon notation is usually used when measuring deviations in isotopic compositions and as these are usually quite small, the epsilon measures the relative deviation in parts of  $10^4$  and will thus have the limits  $[-\infty, 10^4]$ . After a collision the deviation in composition of the resulting planet and Moon can be determined by two simple mass balance equations (Canup 2012):

$$\epsilon_P = \epsilon_{\text{tar}} F_P + \epsilon_{\text{imp}} (1 - F_P), \quad (\text{C.2})$$

$$\epsilon_M = \epsilon_{\text{tar}} F_D + \epsilon_{\text{imp}} (1 - F_D), \quad (\text{C.3})$$

where  $F_P$  and  $F_D$  represent the fraction of target material in the resulting planet and disk.  $\epsilon_P$ ,  $\epsilon_M$ ,  $\epsilon_{\text{tar}}$ ,  $\epsilon_{\text{imp}}$  are the deviations of the resulting planet, Moon, target planet, and impactor. Assuming that the isotopic deviation is spread equally in the silicate material of the planet we can investigate the allowed values for  $\epsilon_{\text{tar}}$  and  $\epsilon_{\text{imp}}$  in a collision. This is because for the Earth-Theia collision the deviations of the resulting planet (Earth) and Moon is known. Setting  $\epsilon_P = 0$  and relating  $\epsilon_{\text{tar}}$   $\epsilon_{\text{imp}}$  we can rewrite Eqs. (C.2) and (C.3) as:

$$\epsilon_{\text{tar}} = -\epsilon_{\text{imp}} \frac{1 - F_P}{F_P}, \quad (\text{C.4})$$

$$\epsilon_M = -\epsilon_{\text{imp}} \frac{\delta f_T}{100}, \quad (\text{C.5})$$

$$\delta f_T = 100 \left( \frac{F_D}{F_P} - 1 \right), \quad (\text{C.6})$$

where  $\delta f_T$  indicates the percentage of silicate material from the target planet in the resulting Earth and disk, and  $\delta f_T = 0$  represents a disk with an equal fraction of target material as in the resulting Earth. This allows one to investigate the allowed  $\delta f_T$  percentages to give the seen isotopic variation between Earth and Moon for different kinds of impactor (Meier et al. 2014; Canup 2012).

We can develop a similar approach to decipher the effect of using a target with several silicate layers. However, for this we have to rewrite Eq. (C.2) in terms of the deviation in the different material layers of the target planets:

$$\begin{aligned} \epsilon_P &= \epsilon_{\text{tar},1} F_{P,1} + \sum_n \epsilon_{\text{tar},n} F_{P,n} + \epsilon_{\text{imp}} (1 - F_P) \\ &= F_P \left( \epsilon_{\text{tar},1} + \sum_n (\epsilon_{\text{tar},n} - \epsilon_{\text{tar},1}) \frac{F_{P,n}}{F_P} \right) + \epsilon_{\text{imp}} (1 - F_P), \end{aligned} \quad (\text{C.7})$$

where  $\epsilon_{\text{tar},1}$  and  $\epsilon_{\text{tar},n}$  represent the deviation from the terrestrial value of the targets main and  $n$ th silicate material.  $F_{P,1}$  and  $F_{P,n}$  are the mass fractions of the main and  $n$ th silicate material that comes from the target planet and ends up in the resulting planet. One can derive a similar expression for  $\epsilon_M$ , which is written in terms of the different disk fractions instead:

$$\epsilon_M = F_D \left( \epsilon_{\text{tar},1} + \sum_n (\epsilon_{\text{tar},n} - \epsilon_{\text{tar},1}) \frac{F_{D,n}}{F_D} \right) + \epsilon_{\text{imp}} (1 - F_D). \quad (\text{C.8})$$

Setting  $\epsilon_P = 0$  and combining these equations leads to:

$$\epsilon_M = \delta_P \left( \frac{\delta f_T}{100} \epsilon_{\text{tar},1} + \sum_n \Delta \epsilon_n \delta_{ndp} \right) \quad (\text{C.9})$$

$$\begin{aligned} \delta_P &= \frac{F_P}{1 - F_P} & \Delta \epsilon_n &= \epsilon_{\text{tar},n} - \epsilon_{\text{tar},1} \\ \delta_{ndp} &= \frac{F_{D,n}}{\delta_P} - \delta_{Pn} (1 - F_D) & \delta_{Pn} &= \frac{F_{P,n}}{F_P}. \end{aligned}$$

Here we decide to dispatch of the epsilon notation and instead rewrite it in ratios as this gives a much clearer picture when dealing with large differences:

$$Q_i = \frac{10^4 - \epsilon_i}{10^4} = \frac{\Delta_i}{\Delta_E}, \quad (\text{C.10})$$

$$\epsilon_{\text{tar},1} = (1 - Q_{\text{tar},1}) \cdot 10\,000, \quad (\text{C.11})$$

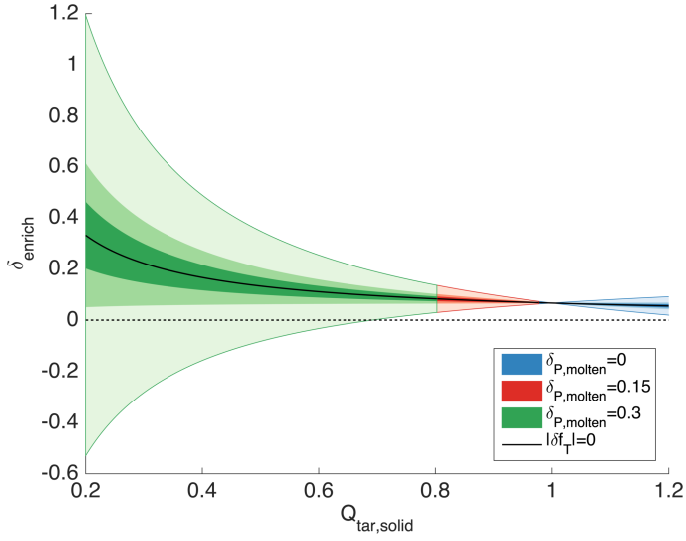
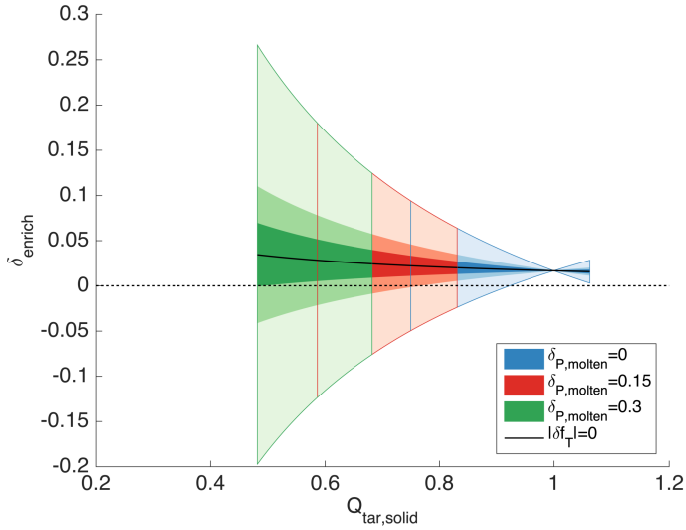
$$\Delta \epsilon_n = \left( Q_{\text{tar},1} - \frac{Q_{\text{tar},1}}{K_n} \right) \cdot 10\,000. \quad (\text{C.12})$$

Here  $K_n$  is the exchange function with respect to material 1:

$$K_n = \frac{\Delta_{\text{tar},1}}{\Delta_{\text{tar},n}} = \frac{Q_{\text{tar},1}}{Q_{\text{tar},n}}. \quad (\text{C.13})$$

The equation then becomes:

$$Q_M = 1 - \delta_P \left( \frac{\delta f_T}{100} (1 - Q_{\text{tar},1}) + Q_{\text{tar},1} \sum_n \left( 1 - \frac{1}{K_n} \right) \delta_{ndp} \right). \quad (\text{C.14})$$

(a)  $\delta\rho=4$ (b)  $\delta\rho=16$ 

**Fig. C.1.** Result of the compositional analysis. The blue, red, and green areas indicate the cases in which the ratios of molten material in the resulting planet are  $\delta\rho_{\text{molten}} = 0, 0.15, 0.3$ , respectively. The vertical red and blue lines represent the extent of the red and blue areas. The light colors represent  $|\delta f_T| < 40\%$ , medium colors represent  $|\delta f_T| < 13\%$ , and dark colors represent  $|\delta f_T| < 6\%$ . The black dashed line highlights  $\delta_{\text{enrich}} = 0$  and the black solid line highlights  $|\delta f_T| = 0$ .